Korean J. Chem. Eng., 38(4), 716-735 (2021)
DOI: 10.1007/s11814-021-0747-y

pISSN: 0256-1115
eISSN: 1975-7220

Bubble dynamics and deformation of free liquid surface in aerated liquid storage tanks

Subhashini Raj Sarath and Janardanan Sarasamma Jayakumar[†]

Department of Mechanical Engineering, Amrita Vishwa Vidyapeetham, Amritapuri, India

(*Received 11 October 2020 • Revised 25 January 2021 • Accepted 26 January 2021*)

Abstract−OpenFOAM was utilized for analyzing bubble behavior and deformation of free liquid surface due to bubble formation and bursting in a rectangular container. Influence of three system parameters, orifice diameter, number of orifices and spacing between orifices, on various bubble dynamics and deformation of gas-liquid interface is presented. The study also incorporates information on bubble formation, bubbling frequency, and orientation of bubbles. Considering different orifice spacing, bubbling synchronicity is also reported. Details regarding interaction of wakes during bubble coalescence for single, double and triple inlet orifices are presented. The deformation of free liquid surface due to bubble formation and bursting is quantified using a new parameter called deformation index (D_L^*). The analyses indicate that the frequency of bubble detachment is augmented with increase in orifice diameter and number of orifices. However, bubble detachment frequency is reduced when orifice spacing increased. Orientation of detached bubbles keeps on changing for larger orifice spacing. Results show that variations of these geometric parameters have substantial influence on free liquid surface deformation due to bubble bursting and other bubble behavior. Using results of these studies, one can develop a bubble-generating device for optimal performance.

Keywords: Bubble Dynamics, Bubble Column, Multiphase Flow, Liquid Surface Deformation, Deformation Index, OpenFOAM

INTRODUCTION

Bubbly flow in various equipment has extensive application in scientific and engineering fields. One such equipment is gas-liquid bubble columns, which are mainly used as multiphase heat exchangers and reactors in chemical, biochemical and petrochemical industries. In addition, bubbly flows have application in various industries for bubbling of gas through liquid that are stored in tank. Such equipment provides many advantages, such as high heat and mass transfer rates, high interphase interaction, compactness, low operating and maintenance cost [1]. Studies of bubble behavior also have applications in other engineering and research fields, such as aeronautics and astronautics, naval, ocean and environmental engineering [2]. Moreover, bubble movement and agglomeration plays an antagonistic role in cavitation erosion that occurs in marine propellers, under water weapons and liquid pump systems in rockets [3]. Even though a number of research studies exist in this field, various bubble dynamics phenomena occurring in bubble columns are still not well explained. Most of the studies deal with only one of the phases, either gas or liquid. In case of gas-liquid bubble columns, research works are oriented towards study of interaction between the two phases. Generation and rise of bubble stir-up the liquid and enhance gas-liquid interaction, thereby causing higher interphase transfer. Study of various bubble behaviors, including bubble coalescence, plays a crucial role for heat and mass transfer in gas-liquid bubble columns and fluidized beds [4]. Therefore, studies of interaction between phases and bubble dynamics and coalescence are very essential and much needed for the optimal design of equipment.

Since density and viscosity ratios are very high in a two-phase gas-liquid system, bubble behavior and its movement are complicated and difficult to predict. Therefore, an accurate and efficient mathematical model is necessary for calculating the bubble rise velocity and various other bubble behaviors. In past decades, wide varieties of techniques were utilized for studying these complex behaviors within the two-phase system. Using the well-known front tracking method, the volume-of-fluid method (VOF) developed by Hirt and Nichols [5], Delnoij et al. [6] numerically investigated the time dependent behavior of gas bubbles. They analyzed and compared formation and rising pattern of skirted bubbles, spherical and cap shaped bubbles. Delaure et al. [7] studied the heat transfer phenomenon due to the movement of bubbles along a surface dipped in hot water. Using particle image velocimetry (PIV) analyses, the authors found that the heat transfer rate was higher at the locations where bubbles showed zigzag motion. In addition, authors numerically studied variations in heat transfer coefficient and the effect of inlet gas velocity on heat transfer rate along the heated surface. Boyce et al. [8] and Wang et al. [9] did a series of analyses in fluidized beds. Using magnetic resonance imaging, Boyce et al. [8] visualized and quantified interaction of bubbles at the time of coalescence within a fluidized bed. Wang et al. [9] carried out experimental analyses to study the bubble dynamics of wet particles in fluidized beds. They concluded that the mechanism of liquid bridge force and the drag force are the main reasons for the change of apparent fluidization of wet particle in a fluidized bed. Wahhab et al. [10] did experimental analyses for predicting the behavior of compressed natural gas (CNG) bubbles within diesel phase. Using a high-speed camera and image processing system, the authors ana-

---

[†] To whom correspondence should be addressed.

E-mail: jsjayan@gmail.com

lyzed variations in bubble shape under the effect of magnetic field. They noted that under the effect of magnetic field, bubble shape changed to elliptical. However, the bubble velocity showed a downward trend with the increase in magnetic field. To study the variations in mass transfer coefficient and distribution of bubble diameter, Arsam et al. [11] did experimental analyses in a large-scale bubble column reactor, using CO, N_2, H_2 and CH_4 for the gaseous phase. They concluded that variations in mass transfer coefficient depend on the bubble size. For analysing bubble behavior within a 2D and 3D two-phase system, Andrzej et al. [12] did numerical studies using ANSYS Fluent. Momentum equation coupled with VOF algorithm was utilized for tracking the gas-liquid interface. Ammar et al. [13] used VOF method for analyzing the bubble behavior within a bubble column. Authors did numerical analyses by using both commercial and open source software (OSS) packages. To study the effect of surface tension on a spherical air bubble within a quiescent liquid phase, Han et al. [14] performed numerical analyses using the VOF method. They observed that five critical Weber numbers (We) exist depending on bubble shape. For studying the effect of bubble movement with heat transfer in a two-phase system within a square duct, Mehta and Khandekar [15] did experimental investigations using infrared thermography. The experimental analyses pointed out that movement of Taylor bubbles had substantial effects in increasing the heat transfer rate across the heated wall. By changing inlet gas flow rate, the authors analysed variations in heat transfer coefficient along the heated wall.

Tariqul et al. [16] investigated bubble behavior such as detachment time, bubble shape and diameter in viscous liquid by varying Reynolds number. Combined volume of fluid and continuum surface force (VOF-CSF) method was used for tracking the interface. Wang et al. [17] performed a two-phase numerical analysis using ANSYS Fluent 14.5. They mainly investigated movement and coalescence pattern of water droplets in oil. For calculating the effect of surface tension force, they used continuum surface stress (CSS) model. By changing the bulk liquid temperature, viscosity and thermal conductivity, they analyzed the axial movement of water droplets, coalescence pattern and behavior. For capturing bubble behavior within a two-phase isothermal system, King and Sadhal [18] conducted numerical and experimental analyses with and without considering surfactant within the bulk liquid. They found that presence of surfactant in the bulk liquid augmented formation of bubble-neck and ultimately the bubble detachment rate was increased. Verma et al. [19] conducted a numerical study on single bubble behavior within a quiescent liquid using open source software OpenFOAM. They analyzed movement pattern and shape change of bubbles within the bulk liquid. VOF method with CSF model were used for interphase reconstruction. Guan et al. [20] also did an almost similar study as that of Verma et al. [19]. By using setField utility, Guan et al. [20] created a 3D bubble. Prasad et al. [21], Raj and Jayakumar [22] did numerical analyses of 2D air-water two-phase systems. For the analyses Prasad et al. [21] used commercial computational fluid dynamics (CFD) software package ANSYS Fluent and analyzed the bubble behavior for a given Weber number and Bond number. However, Raj and Jayakumar [22] used an open source software OpenFOAM and reported the variations of bubble diameter, detachment time and disturbance behavior within the bulk liquid due to bubble movement. They considered different fluid and geometric parameters. Using lattice Boltzmann method (LBM) developed by Chen and Doolen [23] Gupta and Kumar [24] carried out numerical analyses and determined rise velocity of single bubble for different values of Reynolds number (Re), Eötvös number (Eo) and Morton number (Mo). Also for different Eo numbers, the authors analyzed variations in bubble shape. The study showed that as Eo is increased, bubbles deform from spherical to disc. At higher Eo, bubbles deformed into skirt like shape. Rana et al. [25] experimentally analyzed the bursting behavior of Taylor bubbles on free liquid surface within a cylindrical container. The authors compared bursting behavior of bubbles within four different bulk liquids: water, mustard oil, glycerine and silicon oil. Their visualization showed that the bursting time for the Taylor bubble depends on the viscosity of bulk liquid. Due to the low Archimedes number (Ar), the Taylor bubbles within the silicon oil took more time for bursting. For the case of water as the bulk liquid, due to the low Bond number (Bo), higher numbers of stationary bubbles were found in the wake region. Raj and Jayakumar [26,27] using OpenFOAM numerically analyzed the effect fluid parameters such as liquid density and surface tension on bubble behavior. From the numerical investigations they found that with increase in liquid density, equivalent bubble diameter and detachment time were reduced considerably. It was also reported that equivalent bubble diameter and detachment time increased with the increase in surface tension.

Thus, it can be seen that various investigations carried out in the field of bubble dynamics deal with bubble behavior inside a container, which is fully filled with liquid. Most of the numerical investigations mentioned above did not consider presence of the free liquid surface while analysing bubble dynamics. It is also seen that fine details of the bubble dynamics giving an in-depth behavior, where the bubbles emanating from submerged inlets are not reported. In addition, at present there are no numerical studies that consider deformation and busting of bubbles at the gas-liquid interface at the top of the vessel. In this paper, we have quantified deformation of free liquid surface due to the formation and bursting of air bubble by introducing a new parameter. Using VOF and interface compression method, [28,29] the effect of three geometric parameters--orifice diameter, number of orifices and the spacing between orifices on bubble agglomeration--bubble detachment frequency, and deformation of free liquid surface were studied. In addition, variation in bubble detachment time and bubble diameter was also scrutinized. The study also incorporates the information of bubble formation, its orientation and synchronicity of generation. Present work also incorporates details of rising pattern of bubbles immediately after its detachment from triple inlet nozzles, which is also a new result. Details regarding interaction of wakes during the time of bubble coalescence with single, double and triple inlet cases are described. The main purpose of doing these parametric studies was to obtain a better understanding of bubble behavior and free liquid surface deformation due to bubble formation and bursting. So using results of these studies, one can develop bubble-generating devices with optimized performance with minimum conceivable cost. Moreover, the present CFD analysis plays a pivotal role in the design of gas bubble liquid columns with optimized performance, minimum overall dimension with least possible cost.

Numerical analyses were performed using open source CFD code OpenFOAM (Open Field Operation And Manipulation), which is a C++ library consisting of numerous solvers. Present article is organized as follows; the governing equations used in the solver interFoam are described in section 2. Formulation of the solver, details regarding the numerical schemes and the solvers used for solving governing equations are explained in subsection 2.3. Subsection 2.4 incorporates validation details of the solver. Details regarding the physical explanation of the problem, geometry, meshing, boundary conditions and computational details for the present analysis are explained in section 3. Results are presented and discussed in section 4.

METHODOLOGY

1. Governing Equations

Multiphase solver interFoam of OpenFOAM is used for analyzing various bubble dynamics and free liquid surface deformation due to bubbling within the two-phase system. The solver incorporates equations for mixture continuity, momentum and transport equation for phase fraction. The governing equation used for mass, momentum and transport equation for phase fraction for a two-phase system are given below. Governing equation for continuity

$$\frac{\partial\rho}{\partial t}+\nabla\cdot(\rho\vec{\mathbf{V}})=0 \tag{1}$$

where $\vec{\mathbf{V}}$ is the mixed velocity and can be written as

$$\vec{\mathbf{V}}=\vec{\mathbf{V}}_1\alpha_1+(1-\alpha_1)\vec{\mathbf{V}}_2 \tag{2}$$

where α_1 is the volume fraction of phase 1 and can be written as

$$\text{Volume fraction }(\alpha_1)=\frac{\text{Volume of fluid in unit cell}}{\text{Volume of unit cell}} \tag{3}$$

Governing equation for momentum

$$\begin{aligned}\frac{\partial(\rho\vec{\mathbf{V}})}{\partial t}&+\nabla\cdot(\rho\vec{\mathbf{V}}\vec{\mathbf{V}})=-\nabla p_{\_rgh}\\ &+\nabla\cdot[\mu(\nabla\vec{\mathbf{V}})+(\nabla\vec{\mathbf{V}})^T]+\sigma\nabla\alpha_1-\vec{g}\cdot\vec{y}\nabla\rho\end{aligned} \tag{4}$$

where the term $p_{\_rgh}$ represents pseudo or hydrostatic pressure and can be written as follows:

$$p_{\_rgh}=p-\rho\vec{g}\cdot\vec{y} \tag{5}$$

In (5), $\vec{y}$ denotes the position vector and p is the specified total pressure, $\rho\vec{g}\cdot\vec{y}$ is the static pressure.

Solver calculates density and dynamic viscosity values as the weighted average of property values of two phases, as given in (6) and (7).

$$\rho=\rho_1\alpha_1+\rho_2(1-\alpha_1) \tag{6}$$

$$\mu=\mu_1\alpha_1+\mu_2(1-\alpha_1) \tag{7}$$

The transport equation for volume fraction for a two-phase system is

$$\frac{\partial(\rho\alpha_1)}{\partial t}+\nabla\cdot(\alpha_1\vec{\mathbf{V}})+\nabla\cdot[\alpha_1\vec{\mathbf{V}}_r(1-\alpha_1)]=0 \tag{8}$$

where $\vec{\mathbf{V}}_r$ represents the relative velocity between gas and liquid phase which is calculated with (9),

$$\vec{\mathbf{V}}_r=\vec{\mathbf{V}}_1-\vec{\mathbf{V}}_2 \tag{9}$$

$\vec{\mathbf{V}}_1$ and $\vec{\mathbf{V}}_2$ are the velocities of phase 1 and 2.

2. Volume of Fluid (VOF) Method

The volume of fluid (VOF) method works on the principle that the model shares a single set of conservation equation for momentum and equation for volume fraction. Hence, each computational cell is traced out along the entire domain that is considered for the analyses. In this method, fluid phases do not interpenetrate each other and use a function α (x, y, z, t) whose value ranges between one and zero as given by (10) [5,9]. In the present simulation, interface compression scheme was used for the reconstruction. Compared to other interface reconstruction techniques, (piecewise linear interface calculation (PLIC) [9], Donor acceptor [5], flux line-segment model for advection and interface reconstruction (FLAIR) [30], simple line interface calculation (SLIC) [31]), the interface compression scheme is more accurate [5,29-31].

$$\alpha=\begin{cases}0 & \text{In fluid 1}\\ 0<\alpha<1 & \text{Interface}\\ 1 & \text{In fluid 2}\end{cases} \tag{10}$$

Continuum surface force (CSF) [28,32] model is used for calculating the surface tension force within the gas liquid interface. The surface tension force is expressed as volume force by using divergence theorem and is written as follows [2,28,32].

$$F_{vol}=\sigma_{12}\frac{\alpha_1\rho_1 k_2\nabla\alpha_2+\alpha_2\rho_2 k_1\nabla\alpha_1}{0.5(\rho_1+\rho_2)} \tag{11}$$

The curvature at the liquid gas interface is calculated using (12).

$$k_1=k_2=-\nabla\cdot\hat{n}=-\nabla\cdot\left(\frac{\nabla\alpha_1}{|\nabla\alpha_1|}\right) \tag{12}$$

where, $\hat{n}$ is the unit vector normal to the interface.

3. Formulation of the Solver

Numerical analyses were carried out by using multiphase, incompressible, isothermal solver interFoam. The solver incorporates features such as mesh movement and change of mesh topology, including adaptive re-meshing. The solver is based on finite volume method (FVM) and volume of fluid (VOF) with interface compression technique [33,34,36]. Fig. 1 shows the flowchart of the solution procedure used in this numerical study. Details of different discretization schemes and solvers are provided in appendix.

4. Validation of the Solver

For validating the methodology of the solver interFoam, numerical results of the analysis of rising bubble carried out by Zahedi et al. [4] were considered. The authors carried out the numerical analyses using commercial CFD software package ANSYS Fluent 6.3. The geometry with boundary conditions used for the validation case is shown in Fig. 2(i).

The resulting void fraction contours are shown in Fig. 2((ii)(a))

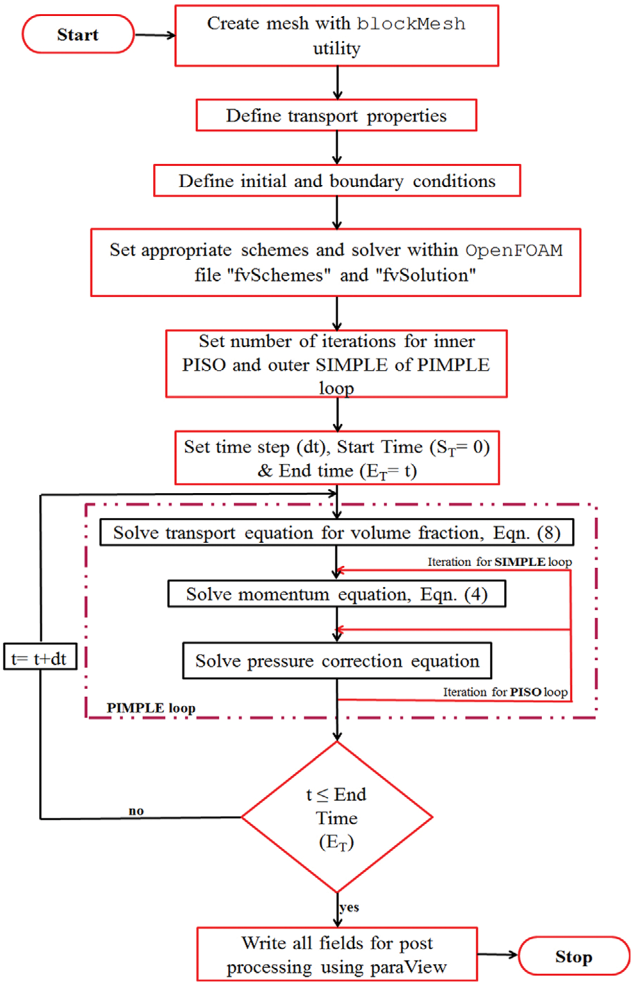

Fig. 1. Solution procedure for the present analyses.

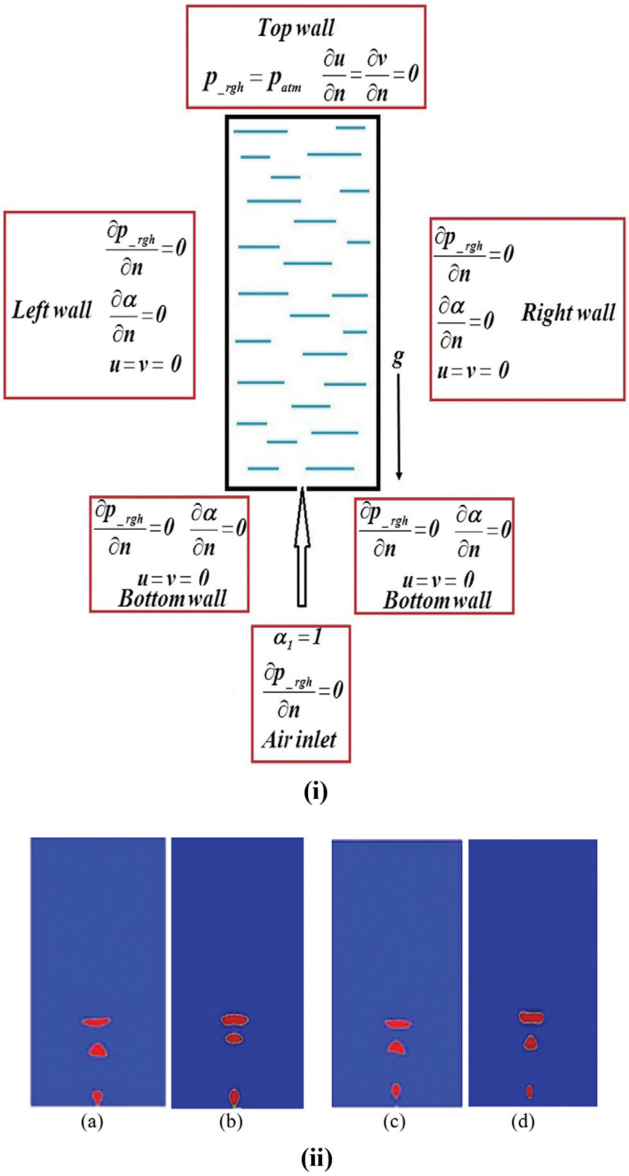

Fig. 2. (i) Boundary conditions for validation. (ii) Comparison of void fractions, t=0.25 s (a) and (c) Zahedi et al. [4], (b) and (d) Present analysis with OpenFOAM; (a) and (b) ρ_l=1,500 kg/m^3, (c) and (d) ρ_l=2,000 kg/m^3.

to (d). These figures show a snapshot of void fraction using two different density values of bulk liquid, 1,500 and 2,000 kg/m^3, for an inlet orifice of 0.5 mm diameter. Qualitative information regarding bubble behavior, such as bubble development, detachment and growth, is portrayed in these figures. On comparison, it is observed that the bubble behavior shows patterns similar to that given by Zahedi et al. [4]. Comparison of contours shows that the bubble edges are accurately reconstructed using the interface compression technique [5,28,29,33,34,36] of OpenFOAM as compared to PLIC [9] method of ANSYS Fluent.

Variation of bubble detachment time for different densities is shown in Fig. 3. The graph shows a downward trend with increase in density. The buoyancy force increases with density, which causes the bubble to detach earlier. From the graph, it is clear that the results of the present analysis using OpenFOAM are in good agreement with the results of Zahedi et al. [4].

To find the accuracy of methodology and suitability of solver interFoam, we also considered experimental results of Zahedi et al. [4] for validation. The authors did their experiments in a glass column with square cross section of sides 10 cm and height 50 cm. The glass column was filled with water up to 10 cm height. Air at a constant flow rate was supplied through an orifice using an air pump. Inlet gas velocity and orifice diameter considered were 3 m/s and 1 mm, respectively. The transport properties used for both phases are given in Table 1.

Table 1. Transport properties of gas and liquid phase used in validation

ρ_g (kg/m^3)	ρ_l (kg/m^3)	μ_g (Pa s)	μ_l (Pa s)	σ_l (N/m)	D$_o$ (mm)
1.225	998.2	1.789e-5	0.001	0.0728	1.0

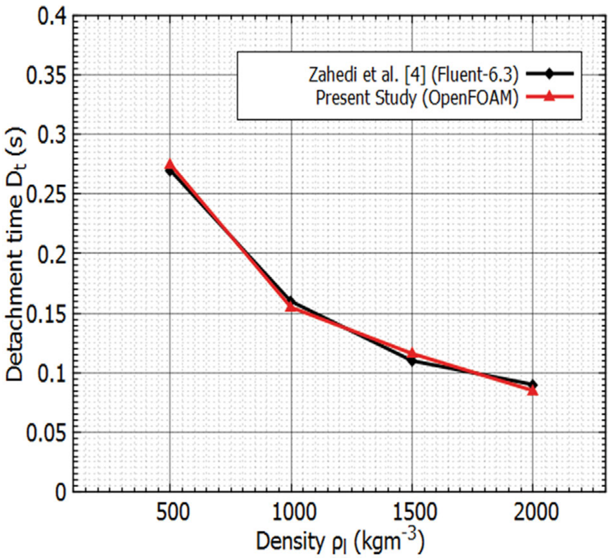

Fig. 3. Variation of bubble detachment time with bulk liquid density.

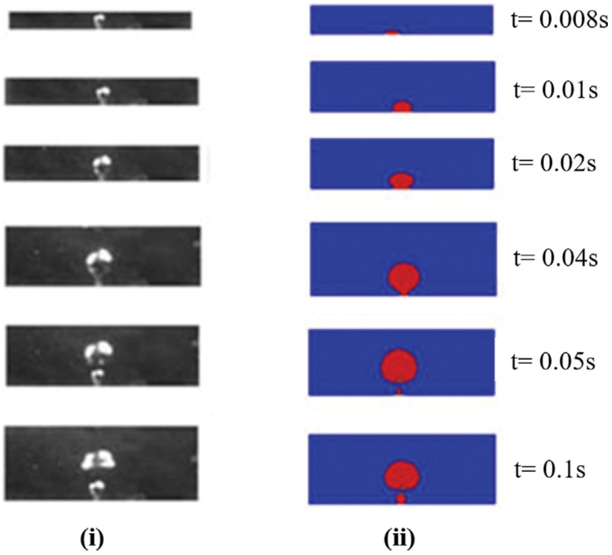

Fig. 4. Comparison of bubble formation and detachment (D_o=1 mm V_g=3 m/s), (i) Experimental analysis, Zahedi et al. [4]. (ii) Numerical results, OpenFOAM.

Fig. 4(i) gives the experimental contours (projection on the XY plane) and Fig. 4(ii) gives the results of numerical simulation using OpenFOAM (2D analysis) of the rising bubble at various time instances. From these results, it can be seen that bubbles displayed almost similar behavior during the time of formation and detachment from the orifice. Measured equivalent diameter of bubble at the time of detachment from experimental analyses was 7 mm [4]. From the OpenFOAM results, the measured equivalent bubble diameter is 7.59 mm [See Fig. 4(ii), t=0.04 s]. On comparing experimental results of Zahedi et al. [4], it is seen that at higher velocity (3 m/s), the relative error is 7.77%. Zahedi et al. [4] compared the experimental results with their numerical analyses (carried out using ANSYS Fluent) and the reported relative error was 8%. That is, as compared to ANSYS Fluent analyses, OpenFOAM analyses show a smaller error.

These results show that the VOF with interface compression technique of OpenFOAM is accurate in tracking and reconstructing the gas-liquid interfaces. Also compared to other interface tracking methods, VOF was found to be accurate. Moreover, since VOF method has lesser computational complexity, it is economical. Numerical validations with Zahedi et al. [4] showed that the relative error percentage with the present analyses was less than 5% and the validation with experimental analysis also showed a good

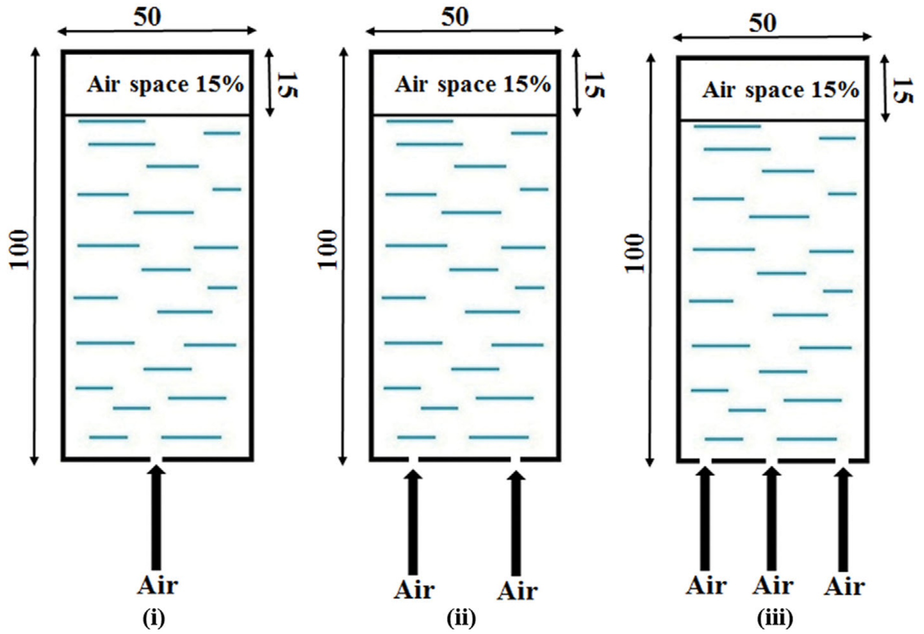

Fig. 5. Computational domain (i) single inlet (ii) double inlet (iii) triple inlet.

matching result. Hence, the multiphase solver interFoam substantiates to be a resourceful and proficient CFD tool for the analysis of present multiphase problem.

ANALYSIS

Working fluids used for these analyses are air (gas phase) and water (liquid phase). Computational analyses were carried out with g (acceleration due to gravity) value of 9.81 m/s^2. The present work considers the effect of different system parameters (orifice diameter, orifice number and spacing between orifices) on bubble formation, bubble dynamics and deformation of free liquid surface due to bubble bursting. To study the effect of orifice diameter on bubble dynamics and free liquid surface deformation, two orifice diameters, 0.3 mm and 0.5 mm, were considered. Considering single, double and triple gas inlets, the effect of number of inlet orifices on bubble behavior and free liquid surface deformation were investigated. Deformation pattern of free liquid surface due to bubble bursting and various other bubble dynamics was investigated by considering three orifice spacings: 12.5 mm, 10 mm and 7 mm. Inlet orifices were kept on either side of the tank axis at equidistance from the center. Transport properties of dispersed and continuous phase considered for analyses are given in Table 1.

1. Computational Domain and Boundary Conditions

Figs. 5(i), (ii) and (iii) show the 2-D rectangular domain having top air space of 15% open to atmosphere with single, double and triple gas inlets. Height and width of the domain was 100 mm and 50 mm, respectively.

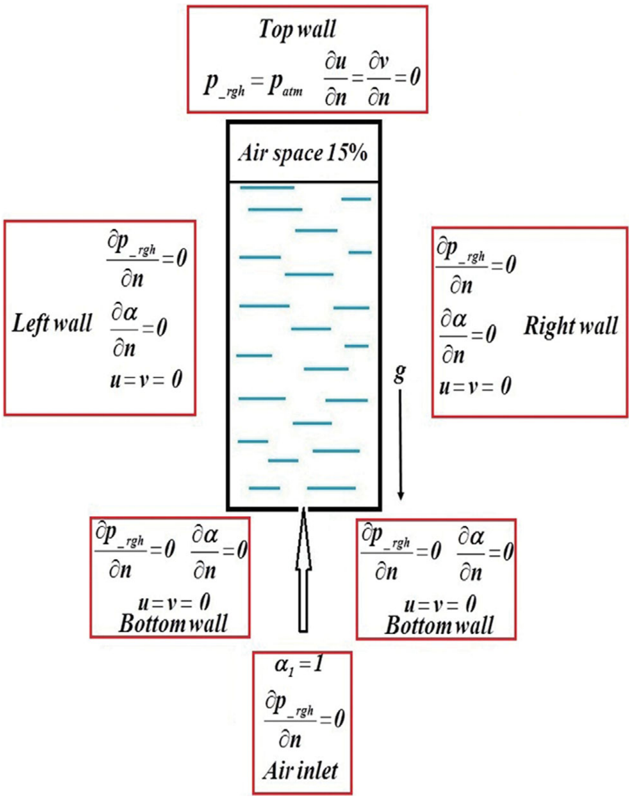

Fig. 6. Computational domain with boundary conditions.

Fig. 6 shows details of boundary conditions used in the analysis. Both gas and liquid phase are initialized as stationary. Since the solver interFoam solves for void fraction for air (*alpha.air*), the value for *alpha.air* is specified as 1 (i.e., filled with air) in the top space and in the remaining portion *alpha.air* is specified as 0 (i.e., filled with water).

A time step of 0.1 ms was used for most of the analysis and in some cases in order to satisfy the Courant Frederick-Levy criteria (CFL) (13) [37], we used a time step of 0.01 ms to 0.02 ms.

$$C = \frac{u\delta t}{\delta x} + \frac{v\delta t}{\delta y} \le C_{max} \tag{13}$$

where u and v are the horizontal (X-direction) and vertical (Y-direction) component of velocities. "δx" and "δy" are the grid size along X and Y direction. δt is the time step. The value of C_{max} depends on the schemes used for solving the discretised equation. For explicit scheme, value for C_{max} will be 1. For implicit scheme, the method is less sensitive to numerical instabilities usually larger values of C_{max} can be accepted.

2. Grid Independence Test

To find the effect of number of cells on the simulation results, grid independence tests were carried out. Four sets of cell numbers (20.10e+04, 50.25e+04, 65.52e+04 and 78.52e+04) were used. The blockMesh utility of OpenFOAM is used for meshing. For the entire analyses, uniform meshing with hexahedral cells are used. Fig. 7 shows the variation of equivalent bubble diameter and time for bubble detachment at different inlet gas velocity with four different mesh densities. From the figures, it is clear that for cell numbers 65.52e+04 and 78.52e+04, the values of equivalent bubble diameter and detachment time are almost same. From the grid independence test, it is observed that the relative precision and accuracy for the bubble behavior are achieved with number 65.52e+04 cells and even if the number of cells is increased beyond 78.52e+04, it does not affect the accuracy of the results. Hence, a computational domain consisting of 65.52e+04 cells is used for single inlet cases.

Similarly, grid independence tests were carried out for double and triple inlet cases. Results show that required accuracy for bub-

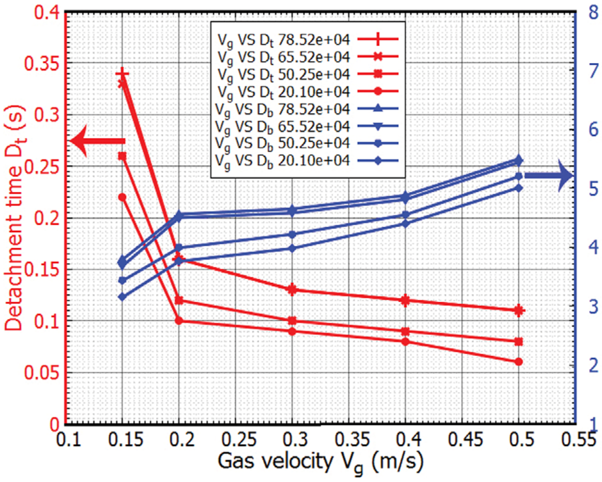

Fig. 7. Grid independency study.

ble diameter and detachment time was attained for 78.52e+04 and 116.87e+04 cells for the double and triple inlets cases, respectively.

3. Computational Details

Computations were carried out on a Dell workstation (Model: Dell precision Tower 7910) with Intel (R) Xenon CPU E5-2680 v3 processor. The CPU speed is 2.50 GHz, the operating system is OpenSUSE Leap 42.3 with 64 GB RAM. Using decomposePar utility of OpenFOAM, 24 processors were used for taking each run. Typical execution time taken for completing one run with 65.52e+04 cells (single inlet cases) is about 55 hours. Whereas for double and triple inlet case with 78.52e+04 and 116.87e+04 cells, the execution time was approximately 90 and 120 hours, respectively. Post processing was done with open source visualization package paraView. By using Visualization Toolkit (VTK) [33,34], paraView processes the data in VTK format to get meaningful results. For graph plotting, software gnuplot was used.

RESULTS AND DISCUSSION

Influence of the three system parameters, orifice diameter, number of orifices and the spacing between orifices, on bubble behavior and deformation of gas-liquid interface are presented discussed.

1. Effect of Orifice Diameter

For investigating the effect of orifice diameter, we considered inlet orifices with 0.3 mm and 0.5 mm diameter. Inlet gas velocities considered were 0.3, 0.5, 0.7 and 0.9 m/s. There are mainly six driving forces that control different stages of bubble growth: bubble formation, neck formation and detachment. The driving forces are pressure force, liquid inertia force, surface tension force, buoyancy force, drag force and the gas momentum force. Out of the above-mentioned forces, the buoyancy, pressure and the momentum force of gas phase control the detachment behavior of bubble from the orifice, and the remaining three forces play an important role in bubble neck formation and subsequent attachment on to the mouth of the orifice. Fig. 8 shows that time required for bubble detachment at different velocities is less for 0.5 mm orifice as compared to 0.3 mm orifice. As the orifice diameter changes from 0.3 mm to 0.5 mm, gas flow rate is increased, thereby increasing the amount of entrapped gas within bubbles. Equivalent bubble diameter values measured at the verge of detachment from the orifice mouth was larger for D_o=0.5 mm as compared to D_o=0.3 mm (Fig. 8). Since equivalent bubble diameters are higher for D_o=0.5 mm, the buoyancy force ($F_b=\rho g \pi R^2$, where R is the bubble radius) on these bubbles will be more as compared to D_o=0.3 mm. Thereby bubble detachment time will be less for cases with D_o=0.5 mm.

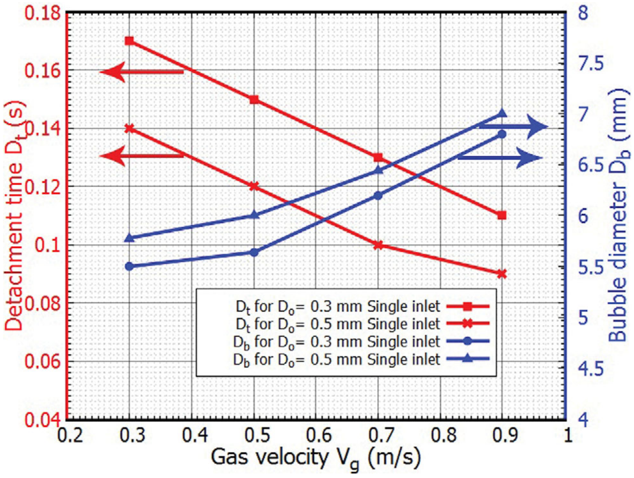

Fig. 8. Bubble detachment time and equivalent bubble diameter considering different orifice size and gas velocity.

It is evident that the bubble behavior at the initial stages (expansion and detachment, Fig. 9(i) to (v)) compares well with the results by Krishna and van Baten [38], and Lin et al. [39]. From Fig. 9(i) to (v) it is seen that, at the time of bubble formation surface tension plays an important role in altering the bubble shape. When the bubble grows (t=0.15 s), as shown in Fig. 9(ii), a neck is formed at the bottom portion of bubble and is at the verge of detachment. Ultimately, the bubble is detached from the orifice (t=0.17 s) under the effect of buoyancy (Fig. 9(iii)). Subsequently, the detached bubble moves upwards (Fig. 9(iv) and (v)). Movement of displaced liquid due to the transverse of bubbles is also shown in Fig. 9.

Figs. 10(i) to (iv) show void fraction contours at different time instants for two orifice diameters and at two gas inlet velocities. On comparing Fig. 10((i)(a)) and Fig. 10((ii)(a)), it is seen that for D_o=0.5 mm, the detached bubble has risen appreciably. However, for D_o=0.3 mm bubble is still in contact with the orifice. At velocity V_g=0.7 m/s, the same trend can be seen (Fig. 10((iii)(a)) and Fig. 10((iv)(a))). From the void fraction contours (Fig. 10((i)(d)) and Fig. 10((ii)(d))) it is seen that, for D_o=0.3 mm at t=0.30 s two bubbles are detached when V_g=0.5 m/s. However, for the same instant, four bubbles are detached for D_o=0.5 mm. For V_g=0.7 m/s and D_o=0.3 mm, at t=0.30 s five bubbles are detached from the orifice. However, at the same time instant, six bubbles are detached for D_o=0.5 mm (Fig. 10((iii)(d)) and Fig. 10((iv)(d))). Hence, from these results it can be stated that for a particular inlet gas velocity, increasing the orifice diameter augments the frequency of bubble detachment. On comparing other time instants for both inlet gas velocities, the number of detached bubbles is more for D_o=0.5 mm. In the case of D_o=0.5 mm for V_g=0.5 and 0.7 m/s, the detached bubbles have larger diameter (Fig. 10((ii)(a)) to (j) and Fig. 10((iv)(a)) to (j)). Since the buoyancy force on detached bubbles corresponds to the bubble size, the detached bubble for D_o=0.5 mm rises faster. It is observed at a lower height the detached bubbles are hemispherical and the bubbles become flatter at subsequent stages of bubble rise (Fig. 10((i)(f)) to (j), Fig. 10((ii)(f)) to (j), Fig. 10((iii)(f)) to (j) and Fig. 10((iv)(f)) to (j)).

To study the moving pattern of the first two bubbles approaching for coalescence, void fraction contours and streamlines are generated. Fig. 11(i) shows the time sequence of bubble detachment from orifice diameter 0.3 mm. At the time of detachment, two velocity components within the bulk liquid play an important role in characterising the size of the bubble neck. The horizontal velocity component compresses the bubble neck, whereas the vertical component has an elongation effect on bubble neck and subsequently the bubble gets detached from orifice. Due to the retardation of surface immediately after the bubble departure from the orifice, the lower part of detached bubble is concave in shape

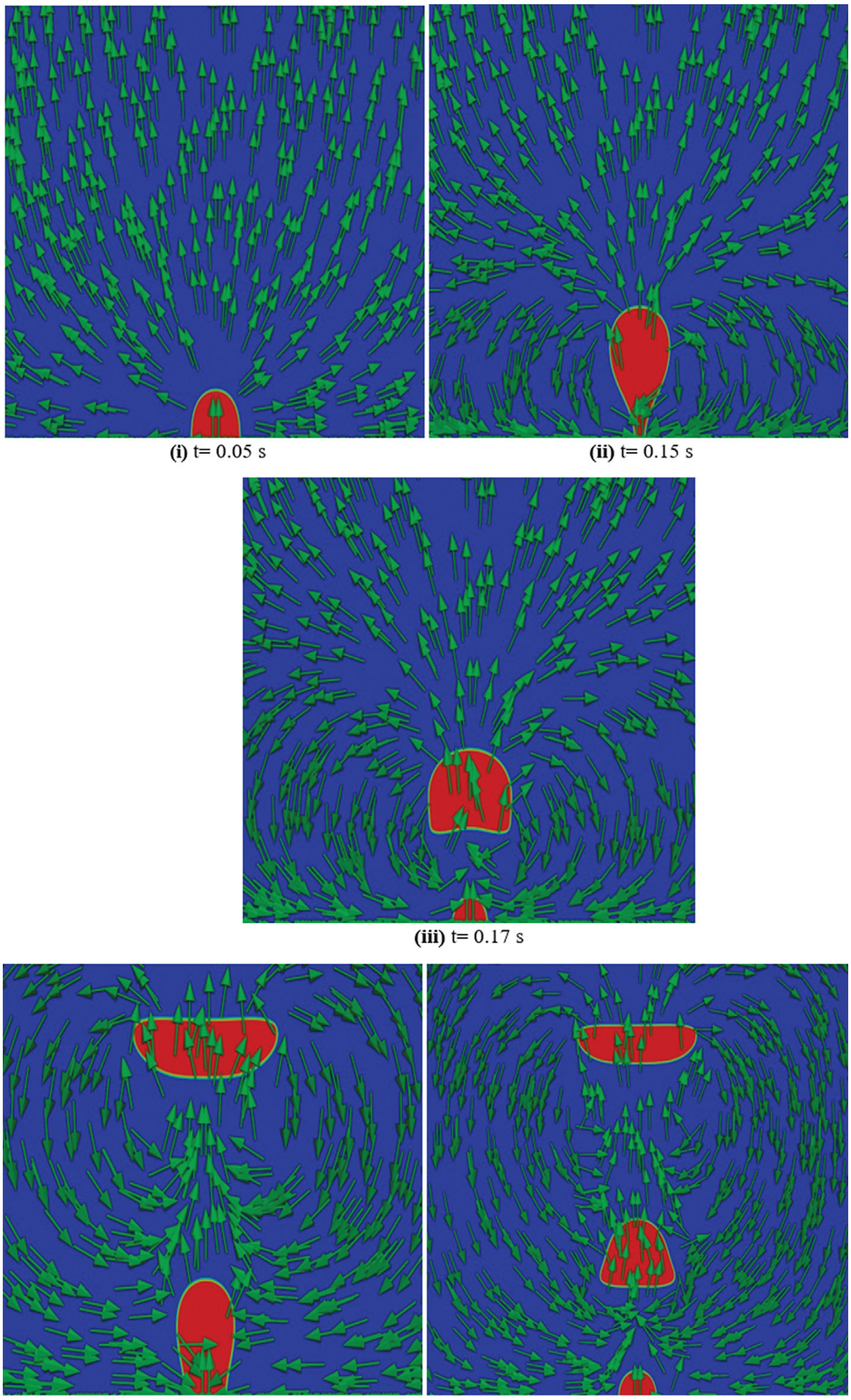

(i) t= 0.05 s **(ii)** t= 0.15 s

(iii) t= 0.17 s

(iv) t= 0.20 s **(v)** t= 0.25 s

Fig. 9. Initial stages of bubble formation (D_o=0.3 mm, V_g=0.5 m/s).

(Fig. 9(iii) t=0.17 s, Fig. 11((i)(b)) t=0.33 s and Fig. 11((i)(c)) t=34 s). The wakes created by the upper (i.e., leading) bubble is shown in Fig. 11((ii)(a))-(e). It is observed that while moving upward, the leading bubbles are deformed more as compared to trailing bubbles. This is because of leading bubbles moving through the dormant liquid. Under the effect of wake, the trailing bubble is accelerated more as compared to upper bubble and merges to form a single bubble. Fig. 12(i) and (ii) show positions of detached leading and trailing bubbles approaching for coalescence at different time instances. Since the graph represents the distance of bubbles

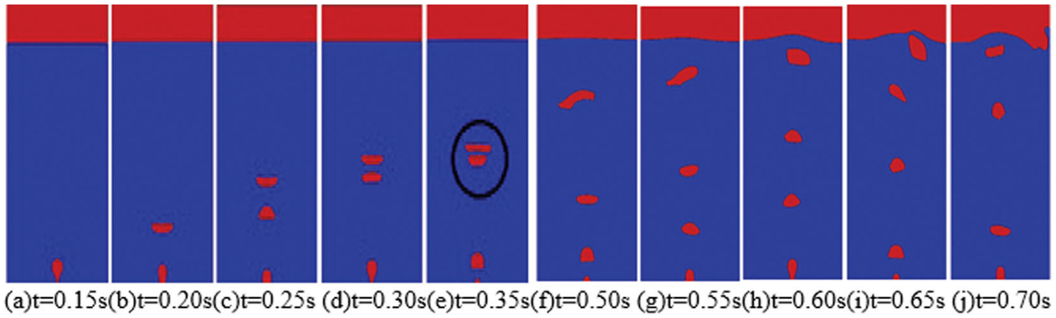

(i) D_o= 0.3 mm, V_g= 0.5 m/s

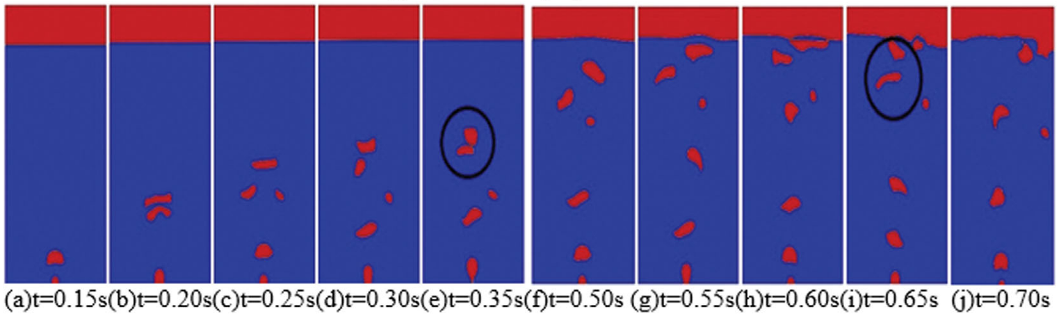

(ii) D_o= 0.5 mm, V_g= 0.5 m/s

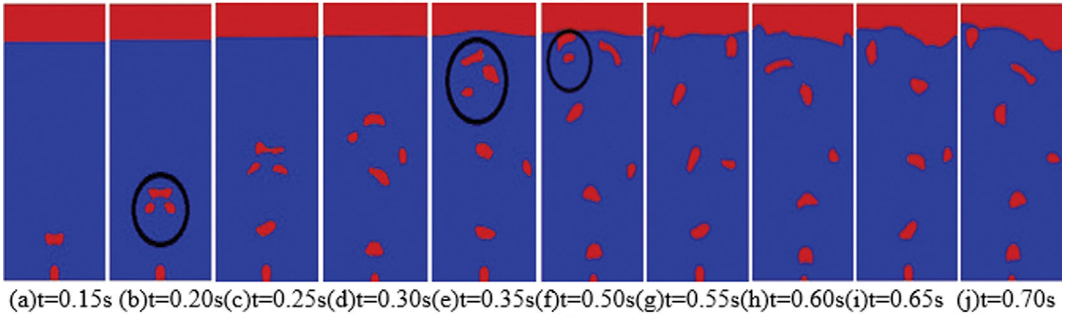

(iii) D_o= 0.3 mm, V_g= 0.7 m/s

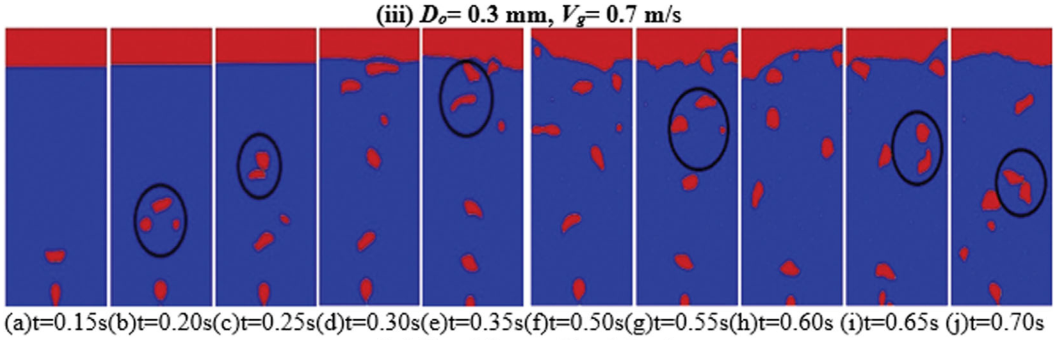

(iv) D_o= 0.5 mm, V_g= 0.7 m/s

Fig. 10. Void fraction contours at different time instant.

at different time instants, the slope of the graph at a given instant gives the bubble velocity at that time. From the graph it can be found that as time increases, due the motion of trailing bubble, distance between bubbles reduces.

For V_g=0.5 m/s and D_o=0.3 mm, only one bubble coalescence is observed between time period 0.15 s to 0.70 s. However, for the same inlet gas velocity, when D_o is changed to 0.5 mm, the number of bubble coalescences increases to two (Fig. 10(i) and (ii)). On comparing Fig. 10(iii) with (iv), it is observed that on changing orifice diameter from 0.3 mm to 0.5 mm, the number of bubble coalescences is increased from three to six (see encircled points in Fig. 10(i) to 10(iv)). It is observed that, at V_g=0.5 m/s and D_o= 0.3 mm, bubble shape becomes more elliptical as the bubble moves towards region near to the top free surface, (Fig. 10(i) and (iii)). However, this trend is not observed at V_g=0.7 m/s with D_o=0.5 mm, (Fig. 10(ii) and (iv)). For the case with V_g=0.5 m/s, orientation of detached bubbles goes on changing as compared to the cases with V_g=0.7 m/s (Fig. 10(i) to (iv)). For V_g=0.7 m/s, top free liquid surface starts to deform during the time of bubble detachment. Deformation of free liquid surface due to bubble bursting is

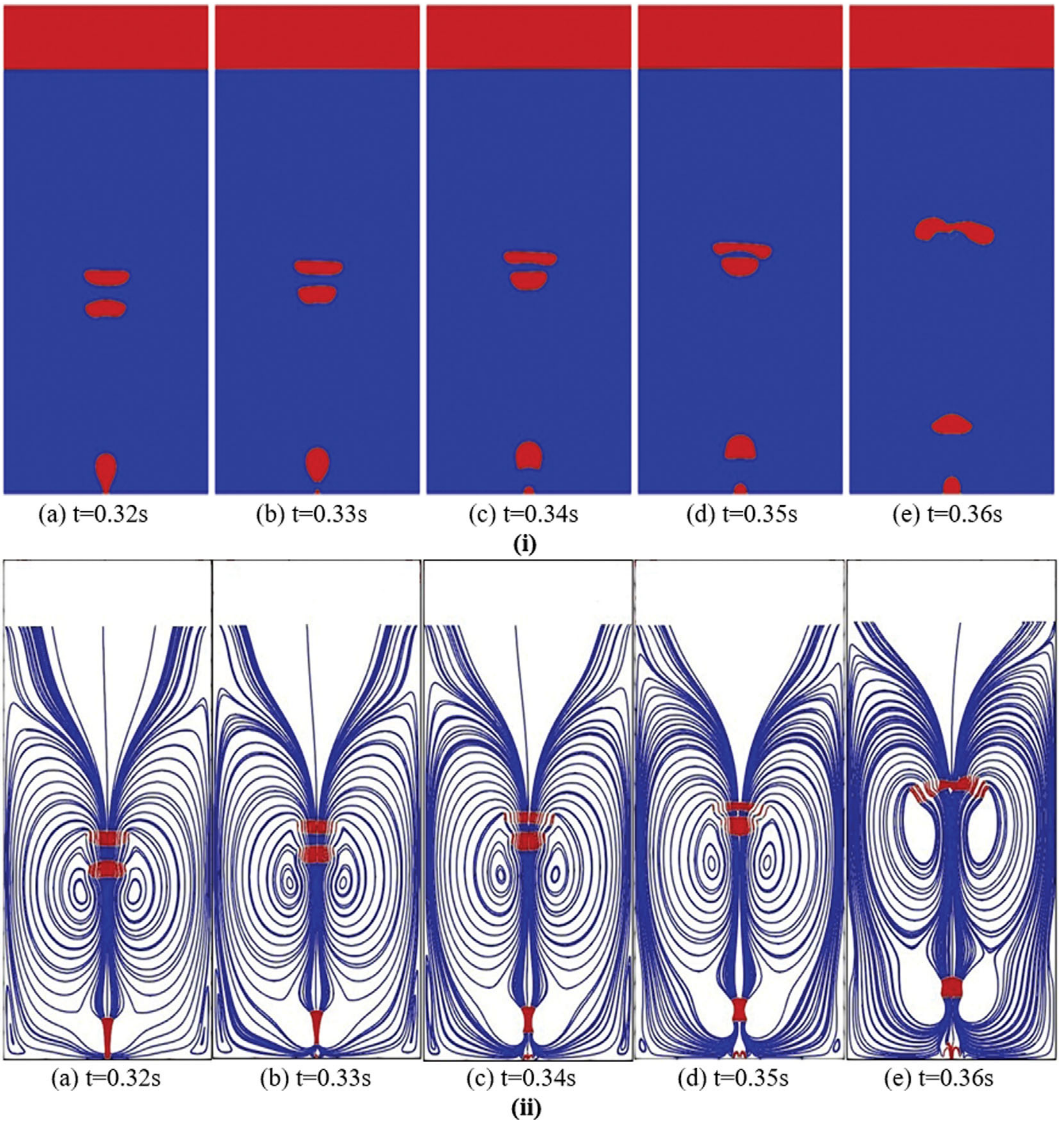

Fig. 11. (i) Void fraction contours of bubble position during the time of bubble coalescence. (ii) Streamline around upward moving bubble (D_o=0.3 mm, V_g=0.5 m/s).

more for the case when V_g=0.7 m/s, (Fig. 10(i) to (iv) and Fig. 13(a) to Fig. 13(d)).

The detachment time (D_t) for D_o=0.3 mm and V_g=0.5 m/s is 0.15 s, whereas D_t for D_o=0.5 mm and V_g=0.5 m/s is 0.12 s (Fig. 8, Fig. 10((i)(a)) and Fig. 10((ii)(a))). For D_o=0.5 mm and V_g=0.5 m/s, first two bubbles approaching for coalescence are seen between 0.17 s to 0.23 s. However, for D_o=0.3 mm and V_g=0.5 m/s, first two bubbles approaching for coalescence are seen between 0.25 s to 0.36 s. Hence from these observations it can be stated that due to the reduction in bubble detachment time, for D_o=0.5 mm, first two bubbles are approaching for coalescence within shorter time interval as compared to cases with D_o=0.3 mm. From Fig. 12 it is seen that for D_o=0.3 mm and at V_g=0.5 m/s, the first two bubbles are about to merge at a height of 0.05 m (Fig. 10((i)(e)) and Fig. 12(i)). For D_o=0.5 mm and V_g=0.5 m/s the first two bubbles are about to merge at a height 0.0295 m (Fig. 10((ii)(b)) and Fig. 12(ii)). The reason for above-mentioned reduction in height is that the detachment time for bubbles is reduced when the orifice diameter is increased. Hence the bubbles detach early from the orifice in the cases of D_o=0.5 mm. Therefore, compared to D_o=0.3 mm, the measured height of first two bubbles approaching for coalescence is lower in the cases of D_o=0.5 mm. For D_o=0.5 mm cases, at region nearer to the free liquid, bubbles with larger diameters are observed (Fig. 10(ii) and (iv)). Therefore, for D_o=0.5 mm, average surface area of bubble interaction with the free liquid surface will be more. Typically, above stated trend of bubble behavior (variations in bubble detachment time and equivalent bubble diameter, bubble detachment frequency, positions and height of first detached bubbles approaching for coalescence) are observed for the cases of V_g=0.3 and 0.9 m/s with orifice diameters 0.3 and 0.5 mm.

As stated earlier, it is seen that there is no study that quantifies the deformation of gas-liquid interface of the free liquid surface. In the present work, along with bubble behavior we have analyzed free liquid surface deformation due to bubble movement and burst-

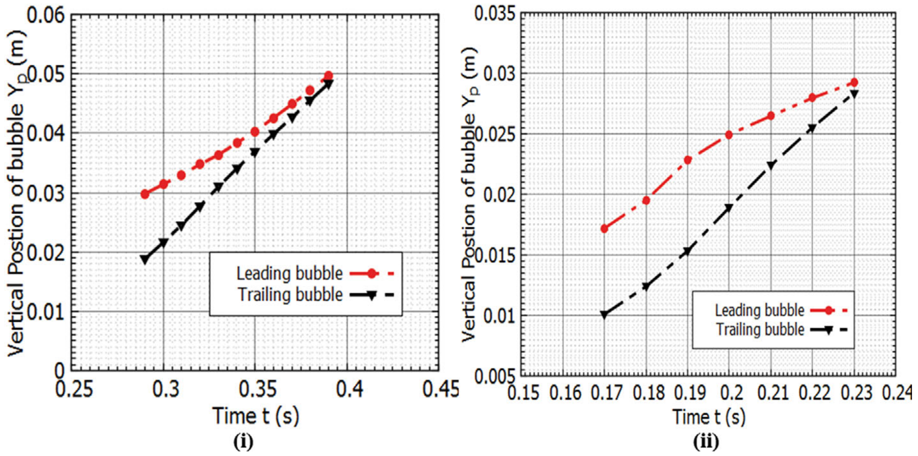

Fig. 12. Position of bubbles approaching for coalescence (V_g=0.5 m/s) (i) D_o=0.3 mm (ii) D_o=0.5 mm.

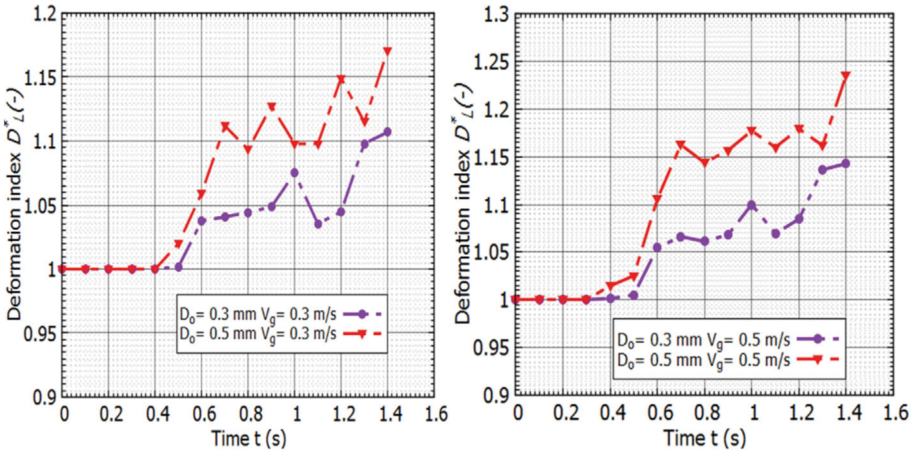

(a) $V_g = 0.3$m/s **(b)** $V_g = 0.5$m/s

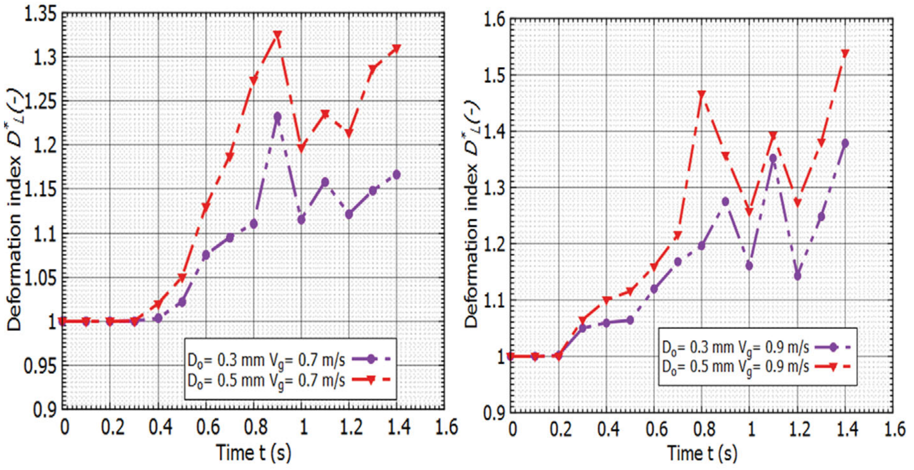

(c) V_g =0.7m/s **(d)** V_g =0.9 m/s

Fig. 13. Variation of D_L^* with D_o.

ing. For quantifying the deformation of free liquid surface, a new parameter called deformation index D_L^* is introduced. The parameter D_L^* is defined as the ratio of developed length of deformed liquid surface at the top air space (D_L) to the diameter (D) of storage tank: $D_L^* = \frac{D_L}{D}$. The developed length of deformed liquid surface at the top air space (D_L) is calculated by summing up the total curvature length of deformed liquid surface. The value of D_L^* will be ≥1.

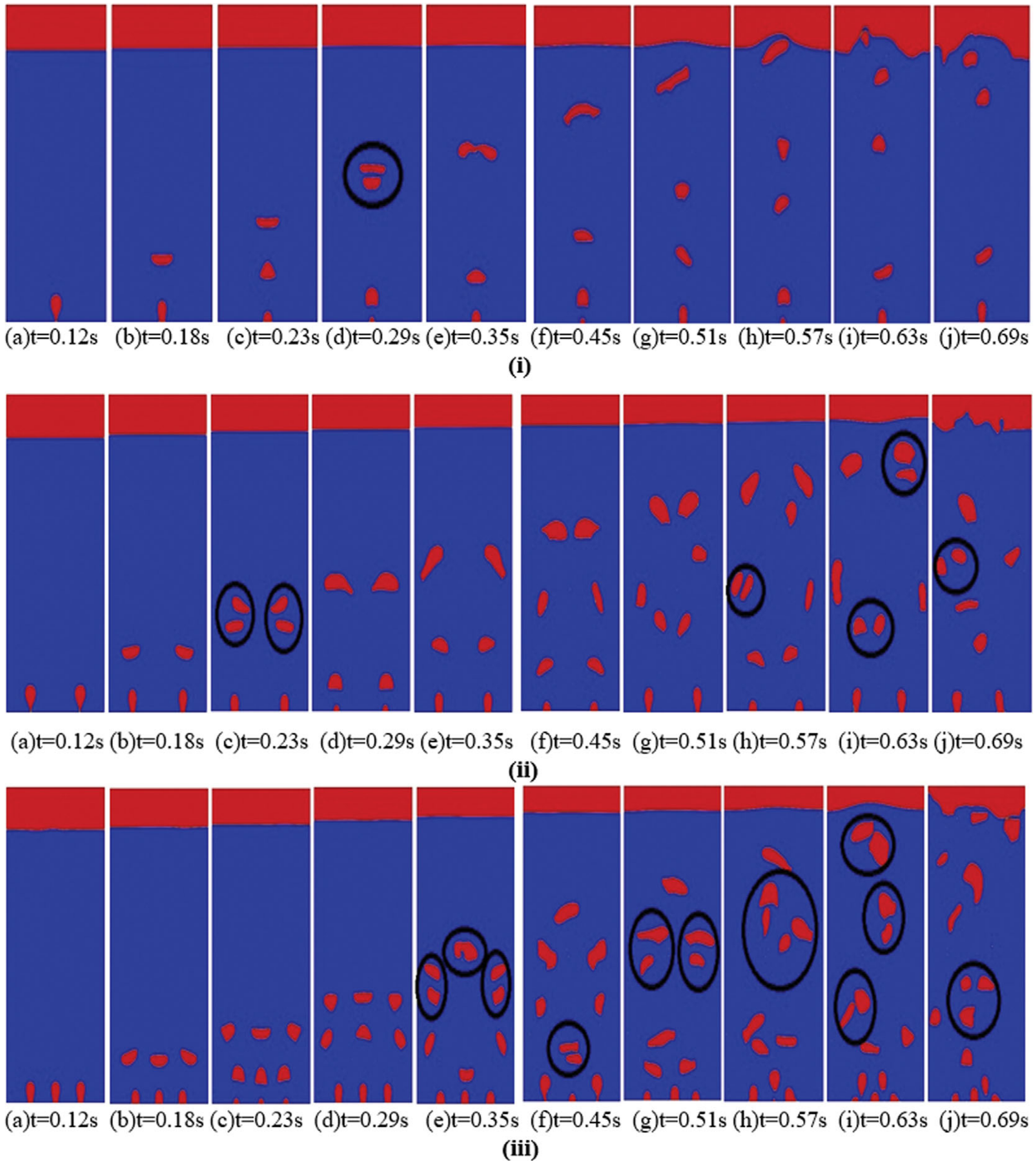

Fig. 14. Void fraction contours at different time instants (D_o=0.3 mm, V_g=0.4 m/s) (i) Single inlet (ii) Double inlet (iii) Triple inlet.

A value of D_L^*=1 indicates there is no deformation on the top free liquid surface, whereas D_L^* value >1 indicates top free liquid surface has undergone deformation. Thus, the dimensionless parameter deformation index D_L^* can be used to quantify the extent of deformation of the free liquid surface.

The variation of D_L^* for two orifice diameters and various V_g values is shown in Fig. 13(a) to (d). It is clear that (Fig. 13(a) and (b)) for D_o=0.3 mm and inlet gas velocities 0.3 and 0.5 m/s, there is no deformation of free liquid surface up to 0.50 s. For the given V_g value, when orifice diameter is changed to 0.5 mm from 0.3 mm, the bubbles near the free liquid surface are larger. Hence, deformation of free surface due to bubble bursting is more for D_o=0.5 mm. However, due to larger bubble diameter for V_g=0.7 and 0.9 m/s, free liquid surface starts to deform during the time of bubble detachment itself. Deformation of free liquid surface due to bubble bursting is more for the cases V_g=0.7 and 0.9 m/s, (Figs. 13(c) and (d)).

2. Effect of Number of Orifices

The effect of number of orifices on bubble behavior and deformation of free liquid surface is discussed in this section. Fig. 14 shows the void fraction contours for single, double and triple inlet cases. Transport properties of gas and liquid phases are kept constant (Table 1).

It is observed that for single and double inlet cases, equivalent bubble diameter at the verge of detachment and time required for detachment are 5.64 mm and 0.12 s, respectively. For double and triple inlet cases, D_b is calculated as the average of equivalent diameters of bubbles generated from each orifice and is represented as D_{bav}. The results indicate that addition of one more orifice does not alter the bubble characteristics, D_b and D_t (Figs. 14((i)(a)) and

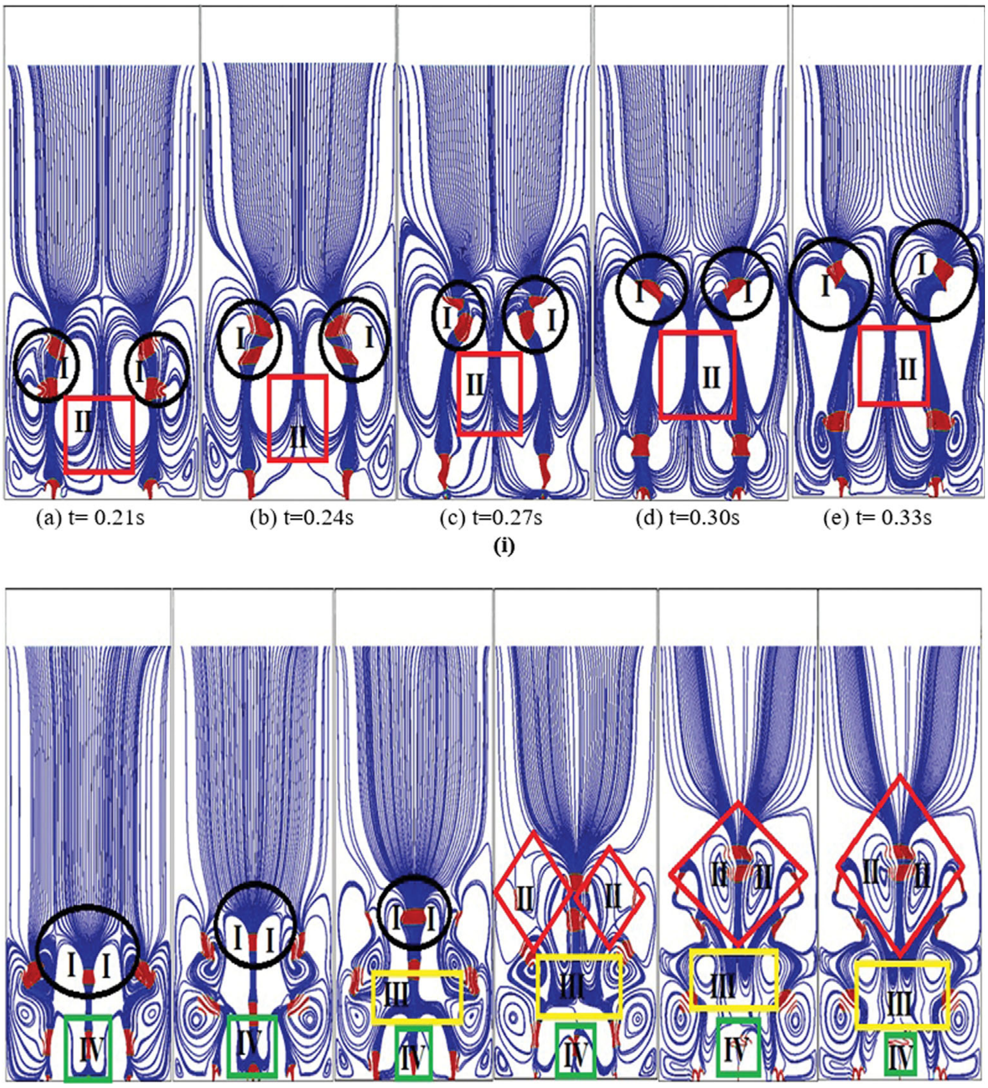

(a) t= 0.21s (b) t=0.24s (c) t=0.27s (d) t=0.30s (e) t= 0.33s

(i)

(a) t= 0.18s (b) t=0.22s (c) t=0.26s (d) t=0.30s (e) t= 0.34s (f) t= 0.38s

(ii)

Fig. 15. (i) Streamlines around bubble, double inlet case with type-I and type-II wake interaction points (ii) Streamlines around bubble, triple inlet case with type-I, type-II, type-III and type-IV wake interaction points (iii) Position of bubbles approaching for coalescence.

((ii)(a))). On comparing Figs. 14((i)(a)), ((ii)(a)) and ((iii)(a)), it is found that for single and double inlet cases, bubbles are at the verge of detachment. However, in the case of triple inlet, the bubble neck is thicker than single and double inlet cases. That is, for triple inlet case, bubbles are not at the verge of detachment but are in expansion stage. Therefore, for triple inlet case the time for bubble detachment is higher, 0.14 s, as compared to single and double inlet cases. Due to this increment in time for detachment, quantity of entrapped air within the bubbles is more. Hence, the D_{bav} for triple inlet case is higher: 5.93 mm.

Let us consider the details regarding bubble agglomeration process for single, double and triple orifice cases. For single inlet case, it is seen that first leading and trailing bubbles are approaching for coalescence between 0.20 s to 0.26 s. The effect of wakes created by the leading bubble and subsequent accelerated movement of trailing bubble for single inlet case is explained in section 4.1. Fig. 15((v)(a)) shows the position of detached leading and trailing bubbles from the bottom wall, approaching for coalescence. It is seen that first bubble coalescence for single inlet case happens at a height of 0.045 m.

Fig. 15(i) shows process of bubble agglomeration for double inlet case. It is seen that due the movement of upper leading bubble, a lesser drag is experienced by the trailing bubble. This causes acceleration of trailing bubble. Hence, the distance between bubbles reduces and subsequently they merge (Fig. 15((iii)(b))). It is observed that, before agglomeration bubbles from the two adjacent orifices move towards the domain axis (Fig. 14(ii) and Fig. 15(i)). After agglomeration, the newly formed bubble moves away from the domain axis. The highlighted oval portions (type-**I** wake interaction) in streamline plot show the wakes created by displaced liquid due to the movement of leading bubble and the sequence of bubble agglomeration process between bubbles gener-

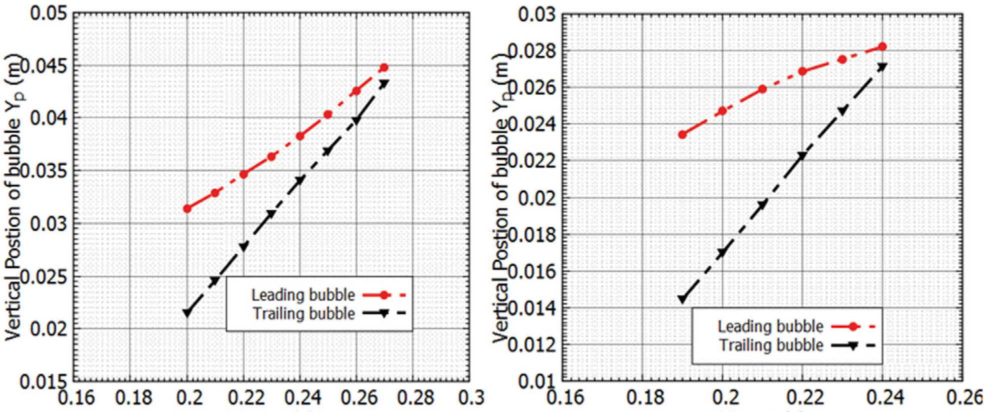

(a) Single inlet (b) Double inlet

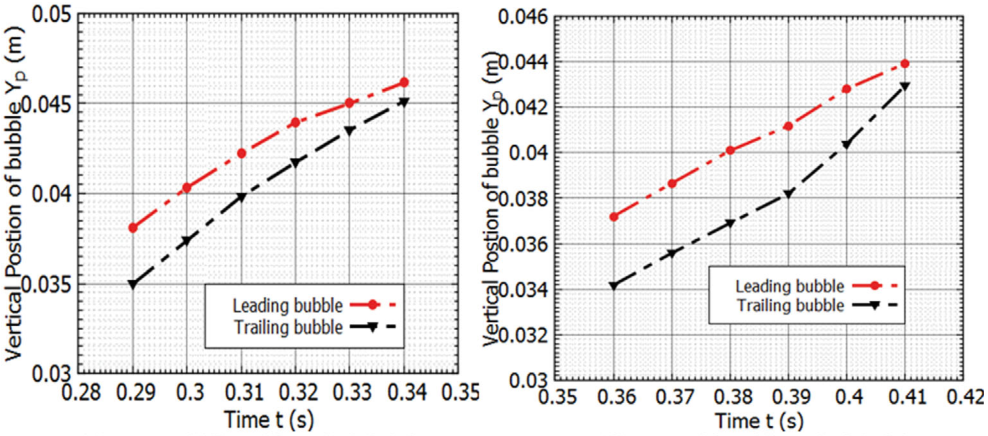

(c) From middle orifice of triple inlet case (d) From side orifice of triple inlet

(iii)

Fig. 15. Continued.

ated from the same orifice. Highlighted square portions (type-**II** wake interaction) show the points of wake interaction created due to the movement of bubbles generated from two adjacent inlets. Due to this wake interaction (type-**II**), bubbles repel horizontally and move towards the wall. Analyses with double inlet show that generated bubbles from adjacent orifices do not merge, i.e., horizontal agglomeration is not observed. However, agglomeration is observed between bubbles generated from the same orifice.

Agglomeration process for triple inlet cases is shown in Fig. 15(ii). It is seen that the elevation of detached leading bubbles from the middle orifice is lower as compared to the elevation of bubbles from side orifices (Fig. 14(iii) and Fig. 15((ii)(a))). The main reason for reduction in elevation is the effect of wakes developed due to the movement of detached bubbles from side orifices. Highlighted oval (type-**I** wake interaction) portions in the streamline plot show the wakes that are created by displaced liquid due to the movement of detached leading bubbles from left and right side orifices. These wakes push the middle bubble downwards (Fig. 15((ii)(a)) and (b)). The wakes created by the emerging bubble from middle orifice push the bubbles from middle orifice to higher altitude. Highlighted rectangular portion (type-**II** wake interaction) shows the wakes generated in the bulk liquid due to the formation of new bubble from middle orifice (Fig. 15((ii)(c)) and (d)). Under the action of this wake, detached second bubbles from middle orifice accelerate more compared to the leading bubbles and ultimately fuse to form a single bubble. The change in positions of leading and trailing bubbles emanating from middle orifice during the process of coalescence is shown in Fig. 15((iii)(c)). It is seen from the figure that the leading and trailing bubbles from middle orifice agglomerate at a height of 0.048 m. Wakes from middle orifice, created during and after the agglomeration process, are shown in highlighted diamond portion (type-**III** wake interaction). At 0.38 s (Fig. 15((ii)(f))), wakes created due to the formation of bubbles after agglomeration push the leading bubbles from side orifices towards the wall. The change in position of leading bubble and trailing bubble during the time of bubble coalescence from side orifice is shown in Fig. 15((iii)(d)). From Figs. 15((ii)(a)) to 15((ii)(f)), the highlighted square portions (type-**IV** wake interaction) show the wakes due to the bubbles, which are in development stage from the middle orifice. This wake is created by bubbles already detached from right and left orifices. Because of this wake, at initial stages, bubbles from middle orifice take slightly more time for detachment. From Figs. 14(i) to (iii) it is seen that, in triple inlet case more bubble coalescences (black encircled points) are present as compared to single inlet case. Number of bubble coalescences in single, double and triple inlet cases, respectively, are 1, 6

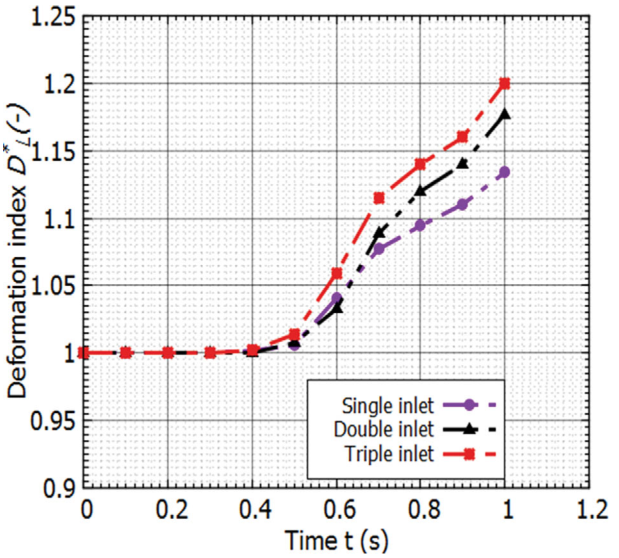

Fig. 16. Variation of D_L^* with single, double and triple inlets.

and 12. It is observed that for single inlet case, bubble shape becomes flatter as the bubbles move towards region near to the gas space (Fig. 14((i)(f)) to (h)). However, this trend is not observed in double and triple inlet cases (Fig. 14((ii)(f)) to (h) and 14((iii)(f)) to (h)). For single inlet case, orientation of detached bubble goes on changing as compared to multiple inlet cases (Fig. 14(i), 14(ii) and 14(iii)). For single, double and triple inlet cases there is noticeable change in bubbling synchronicity [40], i.e., bubbles are formed simultaneously through the orifices at regular intervals.

Quantitative variation of deformation of free liquid surface due to bubble bursting, considering single, double and triple inlet cases, is shown in Fig. 16. It is seen that up to 0.40 s, there is no deformation of the free liquid. For single inlet case, bubble shapes become flatter as they move upwards. Therefore, during 0.45 s to 0.60 s, free liquid surface is deformed more for single inlet as compared to double inlet. From the results of analyses, it can be stated that due to the increase in bubble detachment frequency, the deformation of free liquid surface is greater in the case of triple inlet.

Compared with earlier studies (Ma et al. [2] and Zahedi et al. [4]) which considered single inlet, the present numerical analyses deals with multiple inlets and bubble behavior such as variation in bubble diameter, detachment time, coalescence process, thus providing new results. By plotting streamlines, the effects of wakes on bubble coalescence are explained, which were not available in earlier studies. In the present analyses, repulsive movements of bubbles in double and triple inlet cases due to wake interactions are portrayed, which were not reported earlier. Present work also incorporates the details of rising pattern of bubbles immediately after detachment from triple inlet case, which is also a new result.

3. Effect of Orifice Spacing

In this section, we discuss the influence of orifice spacing on bubble behavior, bubble detachment frequency, synchronicity [40] and deformation of free liquid surface. Keeping the transport properties of gas and liquid constant (Table 1), orifice positions are changed. The values of orifice positions (O_s) considered are 12.5, 10 and 7 mm from the axis of the tank. The two inlet orifices are kept at equidistance from the tank axis. Figs. 17(i) to (v) portray information regarding bubble behaviors such as bubble expansion and detachment. From Fig. 17(i) to Fig. 17(v) it is seen that at the time of bubble formation, surface tension plays an important role in altering the bubble shape. When the bubbles grow, as shown in Fig. 17(ii), at t=0.12 s a neck is formed at the bottom portion of bubble. Ultimately, the bubble is detached from the orifice under the effect of buoyancy (Fig. 17(iii)). Due to the retardation immediately after the bubble breakup from the orifice, the lower part of detached bubble is of concave shape. Subsequently, the detached bubble moves towards the top air space (Fig. 17(iv) and (v)). It is seen that for different orifice spacings (O_s), identical bubbles are developed from orifices. Void fraction for orifice spacing of 12.5 mm indicates that bubbles are under expansion stage. For O_s=10 mm, bubbles are about to detach from the orifice, whereas for orifice spacing 7 mm, bubbles have already detached and risen noticeably. On comparison it is seen that, for O_s=7 mm, during initial stages, six detached bubbles are present and and have risen noticeably. However, the number of detached bubbles is four for spacing 10 and 12.5 mm. When distance between the sidewall and the orifice is large, as in the case of O_s=7 mm, the displaced liquid which is flowing down between the sidewall and the orifice is greater. Thus under the effect of wakes created by this backward flow of displaced liquid, bubbles detach early from the orifice for spacing 7 mm as compared to other two orifice spacings. Hence, from the simulations it can be stated that when the orifice spacing is reduced to 7 mm from 12.5 mm, the bubbling frequency is increased. D_t values for orifice spacing 7, 10 and 12.5 mm are 0.12 s, 0.18 s and 0.18 s, respectively. Since D_t value is lower for smaller spacing, lesser amount of air get entrapped in these bubbles. Therefore, average bubble diameter values (D_{bav}) will be less for smaller spacing values as compared to larger spacing. For the three O_s values (7, 10 and 12.5 mm), the equivalent average bubble diameters are 5.91, 5.95 and 6.23 mm, respectively. It is observed that the orientation of detached bubbles changes for larger spacing (12.5 mm) as compared to smaller spacing (7 mm). However, there no noticeable change in bubbling synchronicity.

For analysing the coalescence behavior, void fraction contours (Fig. 18(i)) and streamline contours (Fig. 18(ii)) are plotted. From Fig. 18(i) it is seen that the leading bubbles are deformed more while moving upward as compared to trailing bubbles. Due the movement of upper leading bubble, lower drag is experienced by the trailing bubble. This will accelerate the trailing bubbles and subsequently bubbles merge. The highlighted oval (type-**I** wake interaction) shows the wake effect and subsequent agglomeration of bubbles generated from the same orifice. For orifice spacing of 10 mm, two bubble agglomerations are observed during the period 0.26 to 0.56 s. Hence for O_s=10 mm, bubble are bigger at 0.56 s as compared to those for O_s=7 mm and 12.5 mm. The wakes created due to the movement of leading bubbles enhances the detachment of newly formed bubbles. Bubbles from both the orifices move towards the axis of the domain (Fig. 18(i)). However, under the repulsive action they do not merge, instead moving towards the wall. The highlighted square (type-**II** wake interaction) portion in streamline indicates the wake development between the bubbles, which moves

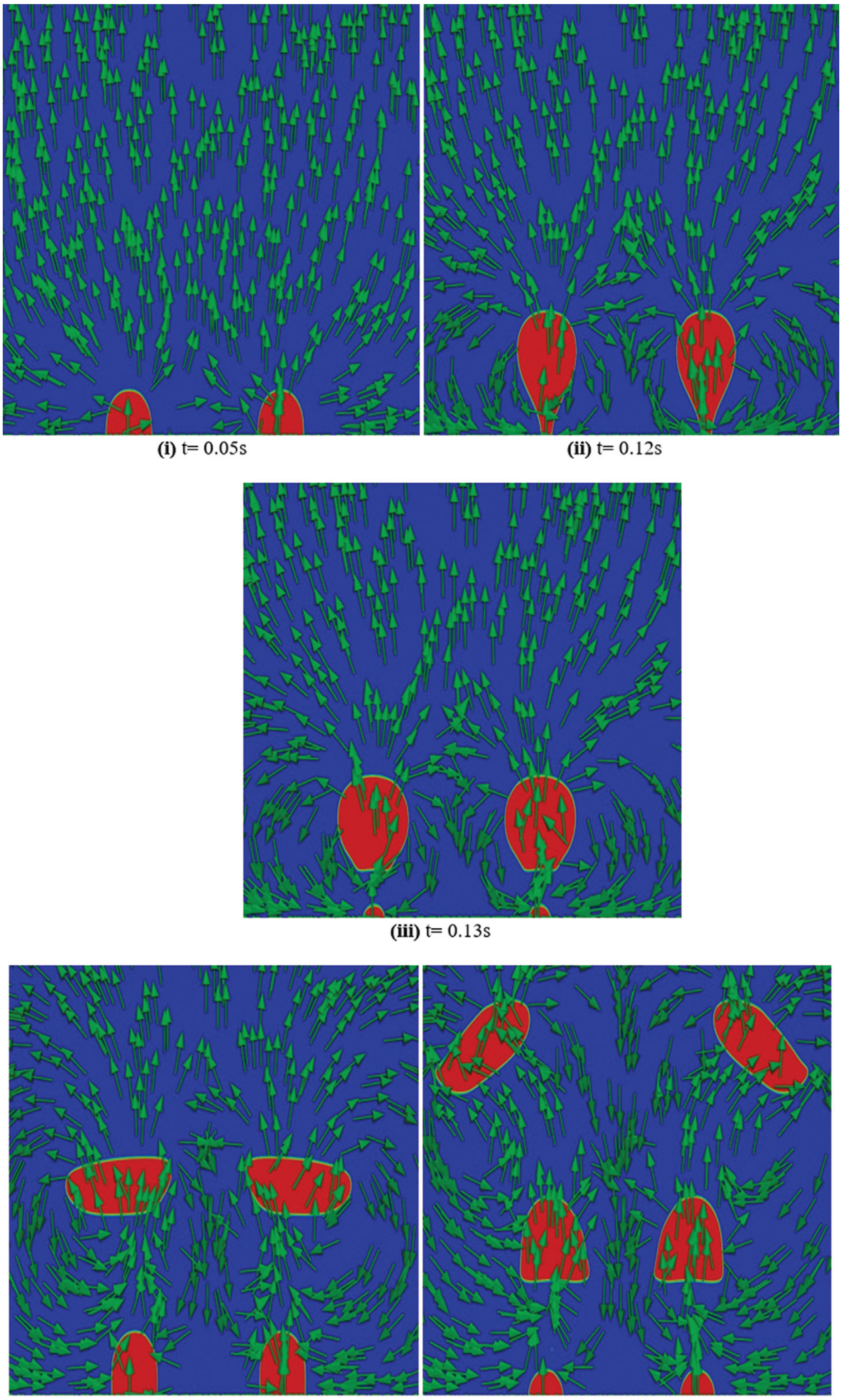

(i) t= 0.05s (ii) t= 0.12s

(iii) t= 0.13s

(iv) t= 0.16s (v) t= 0.26s

Fig. 17. Initial stages of bubble formation, O_s=7 mm.

towards the domain axis. The highlighted rectangle portions (type-**III** wake interaction) in Fig. 18(ii) show the wakes, which are under development stage. These wakes are created due to the bubbles already detached from orifices. These wakes act as driving force for the formation and detachment of newly formed bubbles, which are at the verge of detachment. For orifice spacing of 10 and 12.5 mm, the above-mentioned pattern of bubble movement and wake generations is observed. It is seen that for smaller orifice spacing

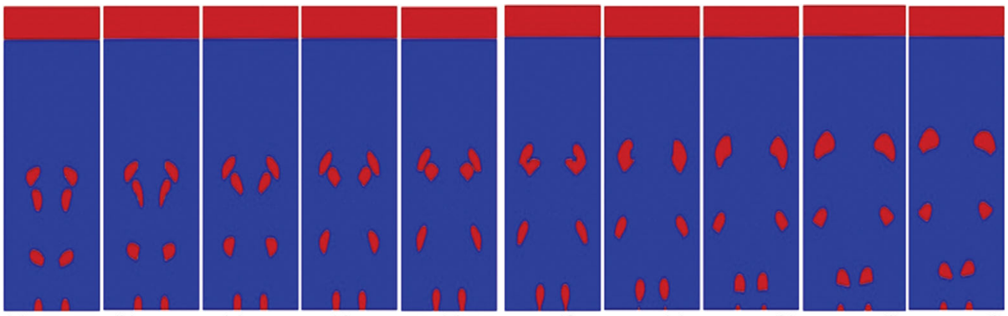

(a) t=0.39s(b) t=0.40s(c) t=0.41s(d) t=0.42s(e) t=0.43s (f) t=0.44s(g) t=0.45s(h) t=0.46s(i) t=0.47s(j) t=0.48s

(i)

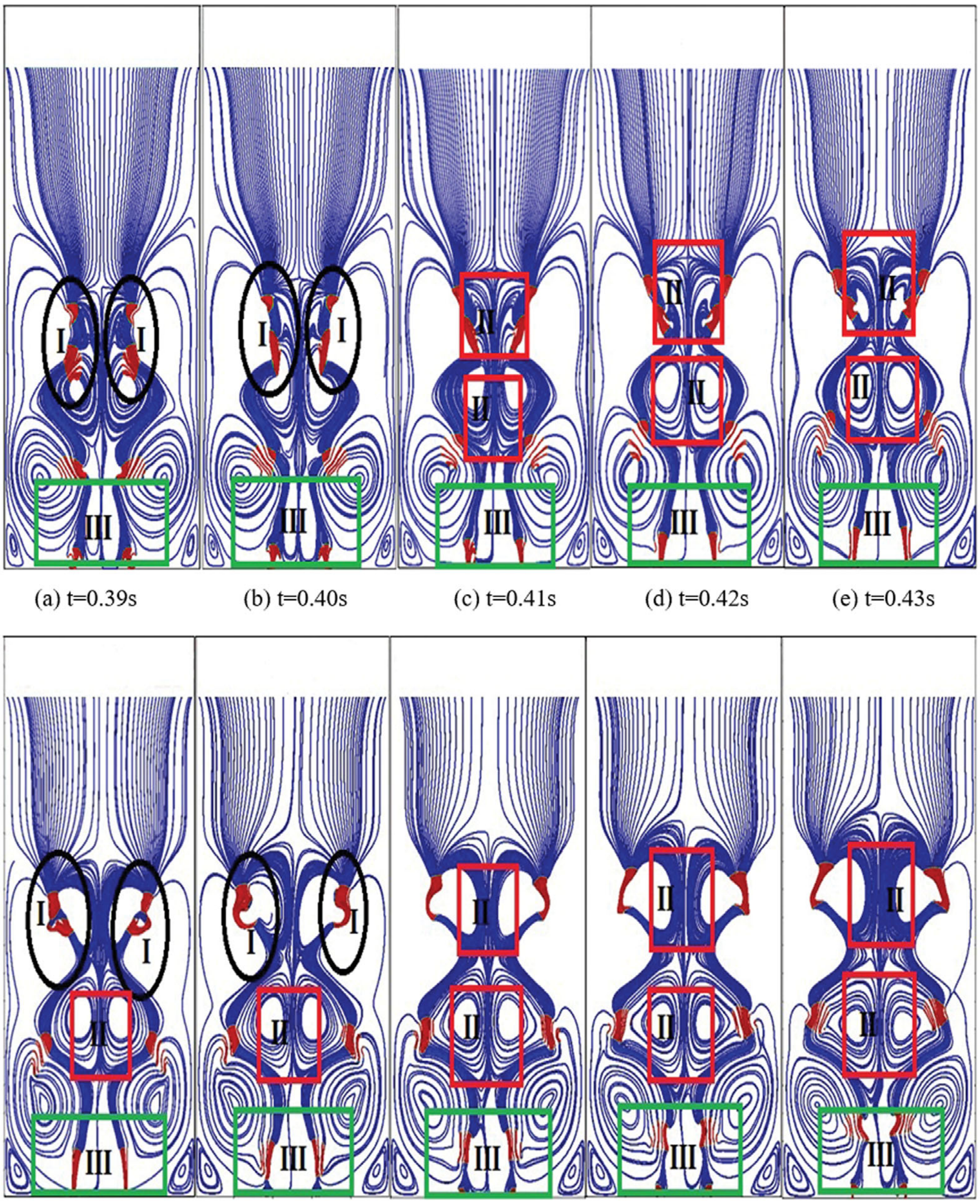

(a) t=0.39s (b) t=0.40s (c) t=0.41s (d) t=0.42s (e) t=0.43s

(f) t=0.44s (g) t=0.45s (h) t=0.46s (i) t=0.47s (j) t=0.48s

(ii)

Fig. 18. (i) Void fraction contours of bubble positions during the time of coalescence. (ii) Streamlines around upward moving bubbles during the time of coalescence with type-I, type-II and type-III wake interaction points.

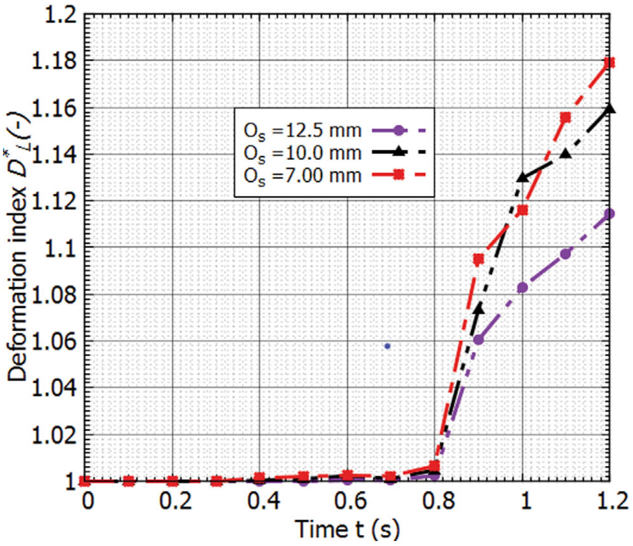

Fig. 19. Variation of D^*_L with different orifice spacing.

(O_s=7 mm), under the action of wakes, bubbles get repelled more and move more towards the sidewall. Nevertheless, for larger orifice spacing (O_s=12.5 mm) similar observations are not seen. From the analysis, for O_s=7 mm first detached leading and trailing bubble merge at a height of 0.043 m. Whereas for O_s=10 and 12.5 mm, these observations are seen, respectively, at a height of 0.0245 m and 0.036 m.

For O_s=12.5 mm, up to time t=0.80 s, there is no deformation of gas-liquid interface at the top air space. However, for orifice spacing 10 and 7 mm, liquid surface is deformed as bubble is approaching towards the free space. For orifice spacing 10 mm, two bubble agglomerations are observed during the period 0.26 to 0.56 s. Hence at 0.56 s, for orifice spacing 10 mm, bubble size is greater as compared to other two orifice spacings. During the period 0.86 s to 1 s, deformation of free liquid surface due to bubble bursting is more for orifice spacing 10 mm (Fig. 19). When the orifice spacing is reduced to 7 mm, the bubble detachment frequency is increased. Hence during t=1.08 s to 1.2 s, deformation of free liquid surface due to bubble bursting is more for orifice spacing of 7 mm (Fig. 19).

The previous studies done by Prasad et al. [21] concentrated only on spacing between orifices as a controlling parameter for the design of bubble generating device (sparger). However, in actual cases orifice size and number also play a pivotal role for the design of spargers in gas liquid bubble column. Apart from orifice spacing analyses, the present work incorporates details of analyses in connection with orifice diameter and number. Therefore, present analyses with different geometrical parameters play an essential role for the design of spargers with optimized performance, minimum overall dimension with least possible cost. In addition, in earlier works, explanation of the bubble coalescence and subsequent interaction of wakes generated due to the movement of bubbles, which are generated either from same orifice or from adjacent orifices, is not available. In the current analyses, we have incorporated details regarding coalescence between bubbles detached from the same orifice and the movement of bubbles towards the axis of domain and subsequent repulsive movement of bubbles under the interaction of wakes.

CONCLUSIONS

The volume of fluid with interface compression method of OpenFOAM was utilized for investigating the dynamics of air bubbles in isothermal liquid pools and resultant deformation of free liquid surface. Studies were carried out by considering different geometric parameters: orifice diameter, number of orifices and its spacing. The solver used for the present simulation was interFoam. The solver and the methodology were validated against published numerical and experimental results. VOF method with the interface compression technique of interFoam was found to be appropriate for present analyses. From the detailed numerical analysis, following conclusions were drawn:

i. As compared to orifice diameter 0.3 mm, time for bubble detachment for different gas inlet velocities was less for orifice diameter 0.5 mm. Bubble diameter at the verge of detachment was larger for D_o=0.5 mm as compared to 0.3 mm. Bubble detachment time was reduced when orifice diameter increased.

ii. To quantify the free surface deformation, a new parameter termed deformation index, D^*_L was introduced. The deformation of free liquid surface (D^*_L) due to bubble bursting was higher for D_o=0.5 mm as compared to D_o=0.3 mm.

iii. Results with single, double and triple inlets showed that when number of orifices was increased from one to two, it did not alter the bubble characteristics D_b and D_t. For both single and double inlet cases, values of D_b and D_t were 5.64 mm and 0.12 s, respectively. However, for triple inlet case D_t and D_b values were higher. The values of D_t and D_b for triple inlet case were 0.14 s and 5.93 mm, respectively.

iv. It was found that due to the increase in bubble detachment frequency, the deformation of free liquid surface (D^*_L) was more for the triple inlet case.

v. Analysis with different orifice spacing indicated that D_t and D_b values increased with increase in orifice spacing. Values of D_t for orifice spacing of 7, 10 and 12.5 mm were 0.12 s, 0.16 s and 0.19 s, respectively. The average bubble diameters for these cases were 5.91, 5.95 and 6.23 mm, respectively. It was also observed that the orientation of detached bubbles goes on changing for larger spacing (12.5 mm) as compared to smaller spacing (7 mm), but there was no noticeable effect in bubbling synchronicity.

vi. For an orifice spacing of 10 mm, two bubble agglomerations were observed during the period 0.26 s to 0.56 s, which was not the case for other two spacings of orifice. Between time t=0.86 s to 1 s, for an orifice spacing of 10 mm, the deformation of free liquid surface due to bubble bursting was more. When the orifice spacing reduced from 12.5 mm to 7 mm, the bubble detachment frequency was increased. Hence, for orifice spacing of 7 mm, deformation of free liquid surface due to bubble bursting is higher.

vii. Analyses indicate that the frequency of bubble detachment is augmented with increase in orifice diameter and number of orifices. However, bubble detachment frequency was reduced when orifice spacing increased from 7 mm to 12.5 mm.

viii. It was found that the time at which first two bubbles begin to agglomerate was reduced with increase in orifice diameter. For double inlet cases, generated bubbles from adjacent orifices did not merge, i.e., horizontal bubble agglomeration was not observed. However, agglomerations were observed for bubbles generated from the same orifice.

ix. For triple inlet case, the first detached leading and trailing bubbles from middle orifice agglomerated at a height of 0.048 m. For triple inlet case, the first detached leading and trailing bubbles from side orifices started to agglomerate only after the agglomerated bubbles from middle orifice moved to a higher altitude.

x. For O_s=7 mm first leading and trailing bubble began to merge at a height of 0.043 m. Whereas, for O_s=10 and 12.5 mm these observations were seen, respectively, at a height of 0.0245 m and 0.036 m.

Using results of these studies, one can develop bubble-generating device with optimized performance, minimum overall dimension and least possible cost. In addition, the present CFD analysis is valuable as it acts as a connecting link of open source software (OSS) based computational analysis in the design of gas-liquid bubble columns.

NOMENCLATURE

Ar : Archimedes number, $\mathrm{Ar}=\dfrac{gL^3\rho_l(\rho_b-\rho_l)}{\mu^2}$ [-]
Bo : Bond number, $\mathrm{Bo}=\dfrac{\rho_l g L^2}{\sigma}$ [-]
C : courant number [-]
D : diameter of storage tank [m]
D_b : equivalent bubble diameter [mm]
D_{bav} : average equivalent bubble diameter [mm]
D_L^* : deformation index, $D_L^*=\dfrac{D_L}{D}$ [-]
D_L : length of deformed free liquid surface [m]
D_o : orifice diameter [mm]
D_t : detachment time [s]
Eo : Eötvös number, $\mathrm{Eo}=\dfrac{\Delta\rho g L^2}{\sigma}$ [-]
E_T : end time [s]
$\vec{F}$: body force at the interface due to surface tension [$\mathrm{Nm^{-2}}$]
g : acceleration due to gravity [$\mathrm{m\ s^{-2}}$]
L : characteristics length [m]
Mo : Morton number, $\mathrm{Mo}=\dfrac{\rho_l\mu_l^4}{\Delta\rho\sigma^3}$ [-]
O_s : orifice spacing [mm]
$p_{\_rgh}$: pseudo or hydrostatic pressure [Pa]
Re : Reynolds number, $\mathrm{Re}=\dfrac{\rho_l VL}{\mu_l}$ [-]
S_T : start time [s]
t/T : time [s]
u, v, w : X, Y and Z component velocities [m/s]
V_g : velocity of gas [$\mathrm{ms^{-1}}$]
We : Weber number, $\mathrm{We}=\dfrac{\rho_l V^2 L}{\sigma}$ [-]
X, Y, Z : cartesian co-ordinates [m]
Y_p : vertical location of the bubble from column bottom [m]

Greek Letters

δx, δy : grid size long X and Y direction [m]
δt : time step [s]
ρ : density [$\mathrm{kgm^{-3}}$]
σ : surface tension [$\mathrm{Nm^{-1}}$]
μ : dynamic viscosity [Pa·s]

Subscripts

1, 2 : fluid 1, fluid 2
av : average
b : bubble/body
g : gas phase
l : liquid phase
max : maximum
o : orifice
p : position
s : spacing

Superscripts

* : dimensionless quantity

REFERENCES

1. N. G. Deen, T. Solberg and B. H. Hjertager, CHISA, *Int. Con. Chem. Pro. Eng.*, Praha, Czech Republic, August 27-31, 1-18 (2000).
2. D. Ma, M. Liu, Y. Zu and C. Tang, *Chem. Eng. Sci.*, **72**, 61 (2012).
3. L. Bin, C. Jun, L. Fengchao and H. Xiulan, *J. Ther. Sci.*, **22**, 352 (2013).
4. P. Zahedi, R. Saleh, R. M. Atanasio and K. Yousefi, *Korean J. Chem. Eng.*, **31**, 1349 (2014).
5. C. W. Hirt and B. D. Nichols, *J. Comput. Phys.*, **39**, 201 (1981).
6. E. Delnoij, J. A. M. Kuipers and W. P. M. van Swaaij, *Chem. Eng. Sci.*, **52**, 3623 (1997).
7. Y. M. C. Delaure, V. S. S. Chan and D. B. Murray, *Exp. Therm. Fluid Sci.*, **27**, 911 (2003).
8. C. M. Boyce, A. Penn, M. Lehnert, K. P. Pruessmann and C. R. Müller, *Chem. Eng. Sci.*, **208**, 1 (2019).
9. H. Wang, A. S. Verdugo, J. Sun, J. Wang, Y. Yang and F. H. Jiménez, *Chem. Eng. Sci.*, **211**, 1 (2020).
10. H. A. A. Wahhab, A. R. A. Aziz, H. H. A. Kayiem and M. S. Nasif, *J. Appl. Fluid Mech.*, **10**, 1649 (2017).
11. B. Arsam, Z. Men, R. I. Juan and B. I. Morsi, *Chem. Eng. Sci.*, **57**, 3307 (2002).
12. K. B. Andrzej, P. M. Machniewski and L. Rudniak, *Poli. Sci. Commi.*, **8**, 17 (2004).
13. A. A. T. Alkhalidi and R. S. Amano, *Water Environ. J.*, **29**, 105 (2014).
14. Y. Y. Han, S. Koshizuka and Y. Oka, *Nucl. Sci. Eng.*, **133**, 192 (1999).
15. B. Mehta and S. Khandekar, *11th Int. Con. Quan. Infr. Ther., QIRT*, 11-14 June, Naples Italy (2012).
16. M. T. Islam, P. Ganesan, J. N. Sahu and F. Hamad, *Ther. Sci.*, **19**, 2127 (2015).
17. Z. Wang, R. Chen, X. Zhu, Q. Liao, D. Ye, B. Zhang, X. He and L. Jiao, *Appl. Therm. Eng.*, **131**, 132 (2018).

18. L. King and S. S. Sadhal, *Heat Mass Transfer.*, **50**, 373 (2014).
19. A. Verma, R. Babu and M. K. Das, *Lect. Notes. Mech. Eng.*, 1059 (2017).
20. H. Guan, J. C. Wang, Z. J. Wei and C. J. Wu, *Appl. Math. Mech.*, **40**, 1181 (2019).
21. V. K. Prasad, D. Chatterjee, S. P. Singh, *SADHANA-ACAD P ENG S*, **43**, 1 (2018).
22. S. Raj and J. S. Jayakumar, *Ind. Soc. Heat Mass Tra.*, 2089 (2017).
23. C. Shiyi and G. D. Doolen, *Ann. Rev. Flu. Mech.*, **30**, 329 (1998).
24. A. Gupta and R. Kumar, *Int. J. Heat Mass Transfer.*, **51**, 5192 (2008).
25. B. K. Rana, L. S. Paikara, A. K. Das and P. K. Das, *Lect. Notes. Mech. Eng.*, 957 (2017).
26. S. Raj and J. S. Jayakumar, *Int. Con. Comp. Meth. Therm. Prob.*, 612 (2018).
27. S. Raj and J. S. Jayakumar, *Lec. Notes. Mech. Eng.*, 769 (2019).
28. J. U. Brackbill, D. B. Kothe and C. Zemach, *J. Comput. Phys.*, **100**, 335 (1992).
29. B. van Leer, *J. Comput. Phys.*, **32**, 101 (1979).
30. N. Ashgriz and J. Y. Poo, *J. Comput. Phys.*, **93**, 449 (1991).
31. D. L. Youngs, *Numer. Methods Fluid Dyn.*, **273** (1982).
32. X. Li, M. Liu, T. Dong, D. Yao and Y. Ma, *Chem. Eng. Res. Des.*, **155**, 108 (2020).
33. C. J. Greenshields, *OpenFOAM User Guide, Version 6.*, (2018) (a). https://cfd.direct/openfoam/user-guide/.
34. C. J. Greenshields, *OpenFOAM Programmer's Guide, Version 6.*, (2018) (b). https://pingpong.chalmers.se/public/pp/public_courses/course09769/published/1558505655816/resourceId/5227641/content/UploadedResources/ProgrammersGuide.pdf.
35. H. K. Versteeg and W. Malalasekera, *An introduction to computational fluid dynamics, the finite volume method*, Second Ed., Pearson Education Limited, England (2007).
36. J. Klostermann, K. Schaake and R. Schwarze, *Int. J. Num. Meth. Flu.*, **71**, 1 (2012).
37. R. Courant, K. Friedrichs and H. Lewy, *Mathe. Anna.*, **100**, 32 (1928).
38. R. Krishna and J. M. Van Baten, *Chem. Eng. Res. Des.*, **79**, 283 (2001).
39. J. N. Lin, S. K. Banerji and H. Yasuda, *Am. Chem. Soc.*, **10**, 936 (1994).
40. S. Xie and R. B. H. Tan, *Chem. Eng. Sci.*, **58**, 4639 (2003).
41. F. Jia, Z. YiLi, Y. H. P. David and C. J. Tsai, *Korean J. Chem. Eng.*, **37**, 423 (2020).

APPENDIX: SOLUTION PROCEDURE

The solution procedure starts with preparation of mesh with blockMesh [33,34] utility of OpenFOAM. Transport properties of gas and liquid phases and the surface tension (μ_g, ρ_g, μ_l, ρ_l and σ) are defined in the file "transportProperties" of OpenFOAM case folder. Initial and boundary conditions for fields such as *alpha.air*, *p_rgh* and *U* are defined in the time directory of the case file. Solution controlling factors such as time step (δt), end time and number of iterations in inner and outer loop of PIMPLE [35] algorithm are specified in files "controlDict" and "fvSolution" [33,34]. The files "fvSchemes" and "fvSolution" within the OpenFOAM case file includes details regarding discretization schemes and solvers used for solving different governing equations. For spatial and temporal discretization, the solver interFoam uses finite volume Gaussian integration and implicit Euler methods, respectively. Interpolation of convective term in the conservation equation for momentum and transport equation for volume fraction is done with limited linear and van Leer schemes, respectively [29,31,33,34,41]. The velocity term is solved using Gauss linear upwind scheme [35]. The surface compression technique [5,29,30,36,41] is used for smoothening the air water interface. The transport equation for volume fraction is solved by using face fluxes of previous time step, pressure and velocity fields. After that, the face fluxes are corrected based on the newly obtained volume fraction values.

While solving the transport equation for void fraction, the boundedness criterion defined by Scarborough [35] is maintained with multidimensional universal limiter with explicit solution (MULES) method [35]. The solver interFoam uses PIMPLE algorithm for pressure-velocity (p-**V**) coupling. PIMPLE algorithm is a combination of semi-implicit method for pressure-linked equations (SIMPLE) [35] and pressure implicit with splitting of operator (PISO) algorithms [35]. To get the time accuracy, the outer loop corrects the pressure equation in three correction steps. The inner loop solves the continuity equation, (1). The file "fvSolution", within the OpenFOAM case directory for present simulation consists of details regarding solvers used for solving the four main equations. The equations are pressure correction equation, first, second, and the last pressure loop and the conservation equation for momentum. Velocity term is solved with smoothSolver and the preconditioner used is symmetric Gauss-Seidel [33-35,41]. The pressure correction is done with preconditioned conjugate gradient (PCG) solver with preconditioner, diagonal incomplete Cholesky (DIC) [33-35,41]. Hydrostatic pressure equation is solved with generalized geometric algebraic multi-grid (GAMG) solver with preconditioner, diagonal incomplete Cholesky (DIC). Thus the temporal and spatial terms are discretized using above-mentioned schemes in the function "*ddt*()", "*div*()" and "*laplacian*()" of "*fvm*" [33,34] class of OpenFOAM. After discretization, a system of equations for each field is obtained which is assembled using "*fvMatrix*" [33,34] class and is solved. This procedure is continued for the specified time (E_t). After reaching the specified end time, the results are post-processed using open source visualization package *paraView* of OpenFOAM [33,34]. The utility foamToVTK of OpenFOAM is used for converting data in native format to VTK format.